

---

# DEEP LEARNING BASED RECONSTRUCTION METHODS FOR ELECTRICAL IMPEDANCE TOMOGRAPHY

---

A PREPRINT

**Alexander Denker**

Department of Computer Science  
University College London

**Fabio Margotti**

Department of Mathematics  
Federal University of Santa Catarina

**Jianfeng Ning**

School of Mathematics and Statistics  
Wuhan University

**Kim Knudsen**

Department of Applied Mathematics and Computer Science  
Technical University of Denmark

**Derick Nganyu Tanyu**

Centre for Industrial Mathematics (ZeTeM)  
University of Bremen

**Bangti Jin**

Department of Mathematics  
The Chinese University of Hong Kong

**Andreas Hauptmann**

Research Unit of Mathematical Sciences  
University of Oulu

**Peter Maass**

Centre for Industrial Mathematics (ZeTeM)  
University of Bremen

## ABSTRACT

Electrical Impedance Tomography (EIT) is a powerful imaging modality widely used in medical diagnostics, industrial monitoring, and environmental studies. The EIT inverse problem is about inferring the internal conductivity distribution of the concerned object from the voltage measurements taken on its boundary. This problem is severely ill-posed, and requires advanced computational approaches for accurate and reliable image reconstruction. Recent innovations in both model-based reconstruction and deep learning have driven significant progress in the field. In this review, we explore learned reconstruction methods that employ deep neural networks for solving the EIT inverse problem. The discussion focuses on the complete electrode model, one popular mathematical model for real-world applications of EIT. We compare a wide variety of learned approaches, including fully-learned, post-processing and learned iterative methods, with several conventional model-based reconstruction techniques, e.g., sparsity regularization, regularized Gauss-Newton iteration and level set method. The evaluation is based on three datasets: a simulated dataset of ellipses, an out-of-distribution simulated dataset, and the KIT4 dataset, including real-world measurements. Our results demonstrate that learned methods outperform model-based methods for in-distribution data but face challenges in generalization, where hybrid methods exhibit a good balance of accuracy and adaptability.

**Keywords** Electrical Impedance Tomography · Image Reconstruction · Deep Learning · Deep Neural Networks

## 1 Introduction

Electrical impedance tomography (EIT) is a well-established imaging modality and is of considerable practical interest in noninvasive imaging and non-destructive testing, with several important medical applications, e.g., monitoring of lung functioning, detection of skin and breast cancer and location of epileptic foci [Holder, 2004]. Further applications arise in geophysics to locate resistivity anomalies, e.g., minerals or contaminated sites [Ellis and Oldenburg, 1994]. The reconstruction problem is to infer the conductivity distribution inside the concerned object from boundary voltage

measurements induced by several injected current patterns. The EIT inverse problem has been intensively studied, and there exists a very rich body of mathematical literature [Borcea, 2002, Uhlmann, 2009], since it was first formulated by Calderón [1980].

This task is mathematically severely ill-posed, meaning that the reconstruction is highly susceptible to the presence of small noise in the data. To deal with the inherent ill-posedness, additional *a priori* information has to be incorporated to allow for accurate reconstructions. Many *model-based reconstruction methods* have been proposed based on variational regularization [Engl et al., 1996, Ito and Jin, 2015], e.g., Sobolev smoothness, total variation and sparsity. These classical regularization functionals, like TV- or sparsity-based Tikhonov regularization, already exploit prior knowledge and promote the desired features, e.g., sparsity of edges or smoothness. Nonetheless, due to the severe ill-posedness and the high degree of non-linearity of the forward model in EIT, the resolution of the reconstructions obtained by these techniques has been modest at best.

The last years have witnessed significant progress in EIT reconstruction regarding both resolution and speed, and there is a fast growing body of literature on *learned reconstruction methods* based on deep learning. This progress is primarily driven by recent innovations in deep learning, especially deep neural network architectures, efficient training algorithms (e.g., Adam [Kingma and Ba, 2015]), and powerful computing facilities, e.g., graphical processing units (GPUs). Conceptually, learning the prior distribution with deep learning models from sufficiently large sets of (paired) training data (if available) potentially offers much greater flexibility than conventional hand-crafted priors, since the data manifold is often hard to capture by explicit mathematical models.

In this work, we investigate the use of deep learning models for EIT reconstruction of experimental data, and conduct a comprehensive comparative study of several representative approaches, including both traditional model-based methods and more recent learned reconstruction methods. There is a fast growing body of literature on deep learning-based approaches for EIT (including reviews, e.g., Khan and Ling [2019]); see Section 4 for detailed discussions. However, most existing studies focus on showcasing the advantages of specific methods, and often compare their performance only with basic model-based methods.

In the last years, several studies have provided comparative studies of deep learning techniques for different tomographic imaging modalities. For example, Leuschner et al. [2021] and Kiss et al. [2025] have evaluated learned reconstruction methods for computed X-ray tomography (CT) using both simulated and real measured data, and have provided valuable insights into the performance of these methods on linear inverse problems. The work that is closest to our study is the recent work by Tanyu et al. [2025], which focuses on deep learning-based EIT reconstruction. While building on similar themes, the present study involves key distinctions. First, we make use of the complete electrode model, which offers a more accurate and realistic representation of the forward process [Somersalo et al., 1992]. Second, we investigate generalization properties of learned approaches by training models on simulated data and testing them on real measured data. This approach mirrors the notorious challenges of data-scarce applications, where large paired datasets are either unavailable or insufficient to train deep learning models accurately. Finally, Tanyu et al. [2025] does not include learned iterative methods [Arridge et al., 2019, Section 5.1.4] in the comparative study, which are often the most effective approach for linear inverse problems in terms of both reconstruction accuracy and generalization. It would be valuable to investigate how these methods perform in the context of nonlinear inverse problem of EIT.

The rest of the survey is organized as follows. In Section 2, we describe the complete electrode model for EIT and relevant mathematical and implementation issues. In Section 3, we provide an overview of classical model-based reconstruction methods, which form the basis of learned approaches and also serve as benchmarks for the latter. In Section 4, we summarize commonly used learned reconstruction approaches and their adaptations to EIT. In Section 5, we provide details on the experimental setup, particularly the dataset used to train the learned reconstruction methods. Finally, in Section 6, we present numerical experiments conducted on both simulated and real data. We conclude the survey with further discussions in Section 7.

## 2 Electrical impedance tomography

Let  $\Omega \subset \mathbb{R}^d$  ( $d = 2, 3$ ) be an open bounded domain representing the concerned object with a Lipschitz boundary  $\Gamma = \partial\Omega$ . In an EIT experiment, one applies an electrical current  $j$  on the boundary  $\Gamma$  and then measures the resulting electrical potential on the boundary  $\Gamma$ . The basic mathematical model, referred to as the continuum model, for the direct problem is the following second-order elliptic partial differential equation (PDE)

$$\begin{cases} -\nabla \cdot (\sigma \nabla u) = 0, & \text{in } \Omega, \\ \sigma \frac{\partial u}{\partial n} = j, & \text{on } \Gamma, \end{cases} \quad (1)$$

where  $n$  denotes the unit outward normal vector to the boundary  $\Gamma$ , and the conductivity  $\sigma$  is assumed to belong to the admissible set

$$\mathcal{A} = \{\sigma \in L^\infty(\Omega) : c_0 \leq \sigma(x) \leq c_1 \text{ a.e. } \Omega\}, \quad (2)$$

where  $c_0, c_1 > 0$  are given numbers. The Neumann boundary data  $j$  should satisfy a compatibility condition  $\int_\Gamma j ds = 0$ . Under the normalization condition  $\int_\Gamma u ds = 0$ , problem (1) has a unique solution  $u$  in  $\tilde{H}^1(\Omega) = \{v \in H^1(\Omega) : \int_\Gamma v ds = 0\}$ . The Neumann to Dirichlet (NtD) operator  $\Lambda_{\sigma,N} : j \mapsto \phi$  maps the Neumann data  $j$  to the Dirichlet data  $\phi = u|_\Gamma$  on  $\Gamma$ . The inverse problem in EIT aims at determining the spatially-varying electrical conductivity  $\sigma$  from the underlying NtD map  $\Lambda_{\sigma,N}$ . This problem was first formulated by Calderón [1980], who also gave a uniqueness result for the linearized problem. The mathematical theory of uniqueness of the inverse problem with the complete NtD map  $\Lambda_{\sigma,N}$  has received enormous attention (see, e.g., Isakov [2006], Uhlmann [2009]). In practice, several input currents are injected, and then the induced electrical potentials are measured (see, e.g., Cheney and Isaacson [1992], Jin et al. [2011] for discussions on optimal input currents), which contains some information about the NtD map  $\Lambda_{\sigma,N}$ . The inverse problem is to determine or at least to approximate the unknown physical electrical conductivity  $\sigma$  from partial knowledge of the NtD map.

Though mathematically well investigated, the continuum model (1) does not capture two of the major complications when dealing with real measurements: (1) The input current is fed into the concerned object via an electrode with a certain spatial extension. For the input on each electrode, we can only have a total current injected on each electrode, and likewise we can measure the voltages on these electrodes. (2) There is a non-negligible contact impedance effect that models the transition of the current from the electrode to the surface of the object. A more realistic mathematical model is the so-called complete electrode model (CEM) [Somersalo et al., 1992], which has been widely used in practical applications, e.g., industrial process tomography [Williams and Beck, 1995], geophysical exploration [Chambers et al., 2007], medical diagnosis [Borsig et al., 2009] and non-destructive evaluation of concrete structures [Karhunen et al., 2010]. Here, a set of  $L$  electrodes is attached to the boundary  $\Gamma$  of the object  $\Omega$ . Then an input current is applied to some subset of these electrodes and the resulting potentials on all the electrodes are recorded, including the ones with applied current. Mathematically, the model reads

$$-\nabla \cdot (\sigma \nabla u) = 0, \quad \text{in } \Omega, \quad (3a)$$

$$u + z_\ell \sigma \frac{\partial u}{\partial n} = U_\ell, \quad \text{on } e_\ell, \ell = 1, 2, \dots, L, \quad (3b)$$

$$\int_{e_\ell} \sigma \frac{\partial u}{\partial n} ds = I_\ell, \quad \ell = 1, 2, \dots, L, \quad (3c)$$

$$\sigma \frac{\partial u}{\partial n} = 0, \quad \text{on } \Gamma \setminus \cup_{\ell=1}^L e_\ell, \quad (3d)$$

where  $\sigma \in \mathcal{A}$  is the electrical conductivity,  $u \in H^1(\Omega)$  is the electric potential, and  $\{e_\ell\}_{\ell=1}^L \subset \Gamma$  denote the surfaces under the electrodes, which are assumed to be mutually disjoint. Further,  $U_\ell \in \mathbb{R}$  and  $I_\ell \in \mathbb{R}$ ,  $\ell = 1, \dots, L$ , are the resulting electrode potentials and applied currents, respectively.

Equation (3b) models the contact impedance effect: When the electrical currents are injected into the object, a thin layer with high resistivity forms at the electrode-electrolyte interface, which causes potential drops at the electrodes as described by Ohm's law. Equations (3c) and (3d) reflect the fact that the current injected through each electrode is completely confined to the electrode, and outside the electrodes there is no current. We denote the space of mean-free vectors by  $\mathbb{R}_\diamond^L := \{x \in \mathbb{R}^L : \sum_{\ell=1}^L x_\ell = 0\}$ . The CEM imposes the conservation of charge (the compatibility condition for the current  $I$ ), i.e.,  $I = (I_1, \dots, I_L) \in \mathbb{R}_\diamond^L$ , and the grounding condition  $U = (U_1, \dots, U_L) \in \mathbb{R}_\diamond^L$  for the electrode voltage  $U$ .

The CEM (3) is described for one single injection pattern  $I \in \mathbb{R}_\diamond^L$ . In practice, several different injection patterns are applied and the respective electrode voltages  $U$  are measured. We denote the electrode voltages and charges for the  $k$ -th injection pattern by  $U^{(k)}$  and  $I^{(k)}$ , for  $k = 1, \dots, K$ , with  $K$  being the total number of injection patterns. Let  $\mathbf{U} = (U^{(1)}, \dots, U^{(K)}) \in \mathbb{R}^{KL}$  and  $\mathbf{I} = (I^{(1)}, \dots, I^{(K)}) \in \mathbb{R}^{KL}$  be the stacked vectors for all electrode voltages and current patterns. Let  $F(\sigma)$  be the forward operator, i.e., the solution map of the CEM for a given  $\sigma \in \mathcal{A}$ , from the injection pattern  $I$  to the electrical voltage  $U$ . Then the EIT direct problem reads

$$F(\sigma)I^{(k)} = U^{(k)}, \quad k = 1, \dots, K,$$

or equivalently  $F(\sigma)\mathbf{I} = \mathbf{U}$ .

The goal of the EIT inverse problem in the context of the CEM (3) is to reconstruct the conductivity  $\sigma$  from the given electrode measurements  $\mathbf{U}$ . In practice, the measured voltages contain noise and below we denote the noisy voltage data by  $\mathbf{U}^\delta$ .

## 2.1 Theoretical background

Now we review relevant theoretical results for the CEM (3). The weak formulation of problem (3) reads: find  $(u, U) \in \mathbb{H}$  such that

$$\int_{\Omega} \sigma \nabla u \cdot \nabla v dx + \sum_{\ell=1}^L z_{\ell}^{-1} \int_{e_{\ell}} (u - U_{\ell})(v - V_{\ell}) ds = \sum_{\ell=1}^L I_{\ell} V_{\ell}, \quad \forall (v, V) \in \mathbb{H}, \quad (4)$$

where the product space  $\mathbb{H} := H^1(\Omega) \otimes \mathbb{R}_{\phi}^L$  is equipped with the norm

$$\|(u, U)\|_{\mathbb{H}}^2 = \|u\|_{H^1(\Omega)}^2 + \|U\|_2^2. \quad (5)$$

Somersalo et al. [1992] showed that for any fixed  $\sigma \in \mathcal{A}$ , there exists a unique solution  $(u, U) \in \mathbb{H}$  to problem (4), and it depends continuously on the current pattern  $I$ . Furthermore, the next theorem by Jin and Maass [2012] gives an improved regularity of the solution. This result can be derived using the Neumann analogue of Meyers' gradient estimates [Meyers, 1963]. The improved regularity plays a crucial role in establishing the differentiability of the forward map.

**Theorem 2.1** (Jin and Maass 2012, Theorem 3.3). *Let  $\lambda \in (0, 1)$ , and  $\sigma(x) \in [\lambda, \lambda^{-1}]$  almost everywhere. Then there exists a constant  $C_1(\Omega, \lambda, d)$ , which depends only on  $\Omega, d$  and  $\lambda$ , such that for any  $q \in (2, C_1(\Omega, \lambda, d))$ , there exists  $C_2 = C_2(\Omega, d, \lambda, q)$  such that the solution  $(u, U) \in \mathbb{H}$  to problem (4) satisfies the following estimate*

$$\|u\|_{W^{1,q}(\Omega')} \leq C_2 \|I\|_2. \quad (6)$$

Due to the change of the boundary conditions between the Neumann and Robin types, the state  $u$  cannot achieve the full  $H^2(\Omega)$  regularity (even if the conductivity  $\sigma$  is smooth). Indeed, near the boundary  $\partial e_{\ell}$  of the electrode  $e_{\ell}$ , the state  $u$  exhibits weak singularities. We refer interested readers to Dardé and Staboulis [2016] for relevant discussions; see Grisvard [1985] for the general regularity theory. To address the limited regularity of solutions in the traditional CEM, Hyvönen and Mustonen [2017] proposed a smoothed version of the CEM. Further, Hyvönen [2004] showed that the CEM can be seen as a Galerkin approximation of the continuum model, and the corresponding current-to-voltage map can be seen as a discrete approximation of the traditional NtD operator  $\Lambda_{\sigma, N}$ .

Due to the finite-dimensionality of the voltage data, the inverse problem in the CEM is inherently ill-posed; however, under certain conditions, uniqueness and stability can still be achieved. For the linearized reconstruction problem in the CEM, Lechleiter and Rieder [2008] proved that for a piecewise polynomial conductivity on a fixed partition, a sufficiently large number of electrodes ensures the unique determination of the conductivity. More recently, Harrach [2019] extended the results to the fully nonlinear case, and proved that the measurements from a sufficiently large number of electrodes uniquely determine the conductivity in any finite-dimensional subset of piecewise-analytic functions. Harrach [2019] also established the Lipschitz stability for the inverse problem under the CEM.

## 2.2 FEM discretization

Since the solution  $(u, U)$  of the CEM (3) is not available analytically, one often uses the finite element method (FEM) to obtain an approximate solution. We briefly recall the FEM discretization following the excellent description in Lechleiter and Rieder [2006]; see Brenner and Scott [2008] for the mathematical theory of the FEM. Specifically, one employs a shape-regular triangulation  $\mathcal{T}$  of the domain  $\Omega$  with  $N$  nodes and defines a finite-dimensional subspace  $V_h$  of the space  $H^1(\Omega)$  to be the set of continuous piecewise linear functions subordinated to the triangulation  $\mathcal{T}$ . We denote by  $\phi_j$  the standard hat function that takes the value 1 at the  $j$ th node and vanishes at all other nodes. Then any function  $u_h \in V_h$  can be represented by

$$u_h(x) = \sum_{j=1}^N \alpha_j \phi_j(x), \quad \alpha_j \in \mathbb{R}.$$

Testing  $(u_h, U)$  in the weak formulation (4) against  $(v, V) = (\phi_i, \mathbf{0})$  yields

$$\sum_{j=1}^N \alpha_j \int_{\Omega} \sigma \nabla \phi_j \cdot \nabla \phi_i dx + \sum_{\ell=1}^L \frac{1}{z_{\ell}} \int_{e_{\ell}} \left( \sum_{j=1}^N \alpha_j \phi_j - U_j \right) \phi_i ds = 0, \quad (7)$$

for  $i = 1, \dots, n$ . Let  $\mathbf{A} \in \mathbb{R}^{N \times N}$  be the admittance matrix and  $\mathbf{B} \in \mathbb{R}^{N \times L}$  defined respectively by

$$A_{i,j} = \int_{\Omega} \sigma \nabla \phi_j \cdot \nabla \phi_i dx + \sum_{\ell=1}^L \int_{e_{\ell}} \frac{1}{z_{\ell}} \phi_j \phi_i ds \quad \text{and} \quad B_{i,\ell} = -\frac{1}{z_{\ell}} \int_{e_{\ell}} \phi_i ds.$$

Then with the vector  $\alpha = (\alpha_1, \dots, \alpha_N)^\top \in \mathbb{R}^N$ , equation (7) can be written as

$$\mathbf{A}\alpha + \mathbf{B}U = 0.$$

Next we take into account the boundary conditions for  $u_h$  arising from the CEM. Testing  $(u_h, U)$  in the weak formulation (4) against  $(v, V) = (0, (\delta_{i,\ell})_{\ell=1}^L)$  (where  $\delta_{i,\ell}$  denotes the Kronecker symbol), we obtain

$$\frac{1}{z_\ell} \int_{e_\ell} \left( U_\ell - \sum_{j=1}^N \alpha_j \phi_j \right) ds = I_\ell \quad \text{or} \quad U_\ell \frac{|e_\ell|}{z_\ell} - \sum_{j=1}^N \frac{\alpha_j}{z_\ell} \int_{e_\ell} \phi_j ds = I_\ell, \quad (8)$$

for  $\ell = 1, \dots, L$ . Upon introducing the diagonal matrix  $\mathbf{D} \in \mathbb{R}^{L \times L}$ , with

$$D_{\ell,\ell} = \frac{1}{z_\ell} \int_{e_\ell} ds = \frac{|e_\ell|}{z_\ell},$$

with  $|e_\ell|$  being the Lebesgue measure of the  $\ell$ th electrode  $e_\ell$ , we may write (8) as  $\mathbf{B}^\top \alpha + \mathbf{D}U = \mathbf{I}$ . Finally, we obtain the linear system

$$\begin{pmatrix} \mathbf{A} & \mathbf{B} \\ \mathbf{B}^\top & \mathbf{D} \end{pmatrix} \begin{pmatrix} \alpha \\ U \end{pmatrix} = \begin{pmatrix} 0 \\ \mathbf{I} \end{pmatrix} \quad (9)$$

for obtaining the FEM solution  $(u_h, U)$  of the forward problem (4). The system has to be augmented with the grounding condition  $\sum_{\ell=1}^L U_\ell = 0$ . One can include this constraint by solving

$$\begin{pmatrix} \mathbf{A} & \mathbf{B} \\ \mathbf{B}^\top & \mathbf{D} \\ 0 & 1 \end{pmatrix} \begin{pmatrix} \alpha \\ U \\ 1 \end{pmatrix} = \begin{pmatrix} 0 \\ \mathbf{I} \\ 0 \end{pmatrix}, \quad (10)$$

where  $\mathbf{1} \in \mathbb{R}^{1 \times L}$  is the row vector with all entries equal to 1. This approach is straightforward to implement but breaks the symmetry and positive definiteness property. Instead, one may consider a Lagrangian formulation for the constraint, which leads to a symmetric and positive definite system. Note that only the stiffness matrix  $\mathbf{A}$  depends on the conductivity  $\sigma$ . That is, we only have to recompute  $\mathbf{A}$  if the conductivity  $\sigma$  changes.

The *a priori* error analysis for the FEM solution  $u_h$  is nontrivial since the solution  $u$  of the CEM does not belong to  $H^2(\Omega)$ . This is due to the possible jumps of the conductivity  $\sigma \in \mathcal{A}$  and because the Neumann boundary values do only belong to  $H^s(\Gamma)$  for  $s < 1/2$ . In order to more effectively resolve the weak singularity of  $u$ , adaptive mesh refinement is a powerful strategy; see Jin et al. [2017], Jin and Xu [2020] for related convergence analysis.

### 3 Model-based reconstruction methods

In this section we describe several model-based reconstruction methods for EIT. These methods roughly can be divided into two groups, i.e., reconstruction methods based on variational regularization (including classical Sobolev smoothness penalty, sparsity and level set method etc.) and direct methods (including D-bar method, factorization method and direct sampling method etc.).

#### 3.1 Variational reconstruction methods

Variational methods are widely employed to reconstruct solutions to ill-posed inverse problems. These methods are generally versatile and applicable to a broad class of inverse problems, and are commonly referred to as Tikhonov regularization [Engl et al., 1996, Ito and Jin, 2015]. The typical strategy is to formulate an optimization problem which minimizes a functional  $J_\alpha$  comprising of a data discrepancy term  $\psi$  and a suitable regularization term  $\mathcal{R}$ , suitably scaled by a regularization parameter  $\alpha > 0$ . The regularization term  $\mathcal{R}$  is used to overcome the inherent ill-posedness, by incorporating prior knowledge on the sought-for conductivity  $\sigma$  into the functional which promotes physically meaningful reconstructions. Common choices for the regularizer  $\mathcal{R}$  include the  $L^2$  and  $L^1$ -norms, or the TV seminorm [Rudin et al., 1992]. For example, the TV penalty is effective for recovering piecewise constant structures and capturing sharp discontinuities, see, e.g., Borsig et al. [2009], Margotti and Hafemann [2022]. One popular choice of the Tikhonov functional is given by

$$J_\alpha(\sigma) = \psi(\sigma) + \alpha \mathcal{R}(\sigma),$$

with the regularization parameter  $\alpha > 0$  balancing the two terms, and the data fitting term  $\psi(\sigma)$  given by

$$\psi(\sigma) = \|F(\sigma)\mathbf{I} - \mathbf{U}^\delta\|_2^2 = \sum_{k=1}^K \|F(\sigma)I^{(k)} - U^{\delta,(k)}\|_2^2.$$

Then one takes a minimizer of the functional  $J_\alpha(\sigma)$  over the admissible set  $\mathcal{A}$  as an approximate solution to the EIT inverse problem. We discuss in detail the sparsity penalty in Section 3.2 below. In practice, the problem has to be further discretized; see [Gehre et al., 2014, Felisi and Rondi, 2024] for convergence analysis of the FEM discretization. For the CEM, the forward map  $F(\sigma)$  is nonlinear in  $\sigma$ , and the functional  $J_\alpha$  is nonconvex and can have many local minima, thereby increasing the difficulty in minimizing the Tikhonov functional  $J_\alpha$ .

To circumvent the nonconvexity, Newton-type methods are often used. These methods involve recursive linearization of the nonlinear operator  $F(\sigma)\mathbf{I}$  around the current iterate  $\sigma_k$ . Let  $F'(\sigma_k)\mathbf{I}$  be the Fréchet derivative of  $F(\sigma)\mathbf{I}$  at  $\sigma_k$ . Then the linearized model is given by

$$F(\sigma_k + \delta\sigma)\mathbf{I} \approx F(\sigma_k)\mathbf{I} + F'(\sigma_k)\mathbf{I}[\delta\sigma], \quad (11)$$

around the current estimate  $\sigma_k$ . Then at iteration  $k$ , the fitting functional  $\psi$  is approximated by a convex quadratic functional

$$\psi_k(\delta\sigma) = \|F'(\sigma_k)\mathbf{I}[\delta\sigma] + F(\sigma_k)\mathbf{I} - \mathbf{U}^\delta\|_2^2, \quad (12)$$

and the Tikhonov functional at the  $k$ th iteration reads

$$J_{\alpha_k,k}(\delta\sigma) = \psi_k(\delta\sigma) + \alpha_k \mathcal{R}_k(\delta\sigma), \quad (13)$$

where  $\mathcal{R}_k$  is a penalization term at step  $k$ , possibly varying with  $k$ . Two commonly used choices are

- $\mathcal{R}_k(\delta\sigma) = \|\delta\sigma\|_{L^2(\Omega)}^2$  for the Levenberg–Marquardt method [Levenberg, 1944, Marquardt, 1963, Hanke, 1997];
- $\mathcal{R}_k(\delta\sigma) = \|\delta\sigma - (\sigma_k - \sigma_0)\|_{L^2(\Omega)}^2$  for the Iteratively Regularized Gauss–Newton (IRGN) method [Engl et al., 1996, Kaltenbacher et al., 2008].

It is a common practice to define  $\psi_k$  using norms different from the original one in order to improve the reconstruction quality or to simplify optimization. The Newton update is computed as

$$\sigma_{k+1} = \sigma_k + \delta\sigma_k,$$

where  $\delta\sigma_k$  minimizes the functional  $J_{\alpha_k,k}$ .

We employ a variation of the IRGN method, or the Gauss–Newton (GN) method. Specifically, we take the penalty  $\mathcal{R}_k$  to be the total variation. In practice, for the discretized problem, we implement a smoothed version of the total variation defined by [Borsig et al., 2009]

$$\mathcal{R}_k(\sigma) = \sum_i \sqrt{(L_i\sigma)^2 + \gamma},$$

where  $L_i$  denotes taking the discrete gradient at the  $i$ th node, and  $\gamma > 0$  a smoothing parameter. Then the update  $\delta\sigma_k$  can be approximated by (with one-step of reweighted least-squares)

$$\delta\sigma_k = (\mathbf{J}_{\sigma_k}^\top \mathbf{J}_{\sigma_k} + \alpha \mathbf{L}^\top \mathbf{D}^{-1} \mathbf{L})^{-1} \mathbf{J}_{\sigma_k}^\top (\mathbf{U}^\delta - F(\sigma_k)\mathbf{I} + \alpha \mathbf{L}^\top \mathbf{D}^{-1} \mathbf{L}\sigma_k), \quad (14)$$

with the diagonal matrix  $\mathbf{D} = \text{diag}(\sqrt{(\mathbf{L}\sigma_k)^2 + \gamma})$  and  $\mathbf{L}$  being the discrete finite difference matrix. Here we identify the function  $\delta\sigma$  with the vector of its coefficients with respect to the given basis. In practice, computing the Jacobian matrix  $\mathbf{J}_{\sigma_k}$  is typically quite expensive and depends on the choice of basis for  $\sigma_k$ . For piecewise constant basis functions, it requires solving  $MK$  PDEs, where  $M$  and  $K$  denote the number of FEM elements (for a piecewise constant representation of  $\sigma$ ) and current patterns, respectively. The method by Polydorides and Lionheart [2002] can reduce the computational burden, requiring the solution of only  $K + L$  PDEs, where  $L$  represents the number of electrodes; see e.g., [Margotti, 2015, Sec. 5.2.1].

Iterative regularization methods for linear problems, e.g., gradient method and iterated–Tikhonov method, can be used in place of the Tikhonov method (13) to define an inner iteration that approximates a minimizer of the linearized problem (12) with suitable accuracy. This idea forms the foundation of the inexact Newton method known as REGINN [Lechleiter and Rieder, 2010, Margotti, 2015, Rieder, 1999, Margotti, 2018]. Alternatively, one can apply gradient type methods directly to the functional  $J_\alpha$  in order to get an approximate minimizer [Engl et al., 1996, Sec. 11.1]. Then regularization may be achieved by prematurely terminating the iteration, using an appropriate stopping criterion, e.g., discrepancy principle [Engl et al., 1996, Ito and Jin, 2015].

One drawback of REGINN is its high computational cost, especially the computation of the Jacobian, which can make them slow for large-scale problems. To address this issue, one-step methods have been proposed, which employ a single iteration of a regularization scheme to compute an approximation. One classical example is the Linearized Reconstruction (LR) method, which performs one Newton step (at an initial guess  $\sigma_0$ ). The LR method can also be

interpreted as the first iteration of the LM or IRGN methods, with a suitable choice of the regularization functional  $\mathcal{R}$ . A well-known variant of the LR method is the NOSER algorithm [Cheney et al., 1990], which was specifically developed for EIT and incorporates a tailored regularization strategy for the context.

In the numerical experiments in Section 6, we employ the following version of the LR method for the discretized problem: we linearize the nonlinear forward operator  $F$  around a homogeneous background conductivity  $\sigma_0$  and reconstruct a perturbation  $\delta\sigma$  relative to  $\sigma_0$  [Cheney et al., 1990, Dobson and Santosa, 1994, Kaipio et al., 2000]. This results in the data-fidelity  $\|\mathbf{J}_{\sigma_0}\delta\sigma - (\mathbf{U}^\delta - F(\sigma_0)\mathbf{I})\|_\Sigma^2$ , under an additive Gaussian noise model  $\mathcal{N}(\mathbf{0}, \Sigma)$ . Then we discretize the perturbation  $\delta\sigma \in \mathbb{R}^M$  using  $M$  coefficients of a piecewise constant finite element expansion, and use the standard Tikhonov regularization, i.e.,  $\mathcal{R}(\delta\sigma) = \|\mathbf{R}\delta\sigma\|_2^2$ , with  $\mathbf{R} \in \mathbb{R}^{M \times M}$  being the regularizing matrix. Then the solution  $\widehat{\delta\sigma}$  is given by

$$\widehat{\delta\sigma} = (\mathbf{J}_{\sigma_0}^\top \Sigma^{-1} \mathbf{J}_{\sigma_0} + \alpha \mathbf{R}^\top \mathbf{R})^{-1} \mathbf{J}_{\sigma_0}^\top \Sigma^{-1} (\mathbf{U}^\delta - F(\sigma_0)\mathbf{I}). \quad (15)$$

Note that the matrix  $(\mathbf{J}_{\sigma_0}^\top \Sigma^{-1} \mathbf{J}_{\sigma_0} + \alpha \mathbf{R}^\top \mathbf{R})^{-1}$  can be computed *a priori*, leading to a computationally cheap reconstruction method, which is necessary for efficiently training post-processing methods (cf. Section 4.2). Further, the Jacobian  $\mathbf{J}_{\sigma_0}$  only has to be computed once, in contrast to the IRGN method. We use a smoothness prior, i.e.,  $\mathbf{R}^\top \mathbf{R} := \Sigma_{SM}^{-1}$  with  $(\Sigma_{SM})_{i,j} = a \exp(-\|x_i - x_j\|_2^2/(2b)^2)$  with  $x_i$  and  $x_j$  being the positions of the mesh elements  $i$  and  $j$ , with  $a = 0.15^2$  and  $b = 0.2$ .

### 3.2 Sparsity reconstruction

The concept of sparsity is highly effective for modelling conductivity distributions that deviate from a known background  $\sigma_0$ , particularly when  $\sigma$  consists of a largely homogeneous background with a few localized inclusions. Let  $\delta\sigma^\dagger = \sigma^\dagger - \sigma_0$ , where  $\sigma^\dagger$  is the exact conductivity. Then we assume that  $\delta\sigma$  admits a sparse expansion with respect to a chosen basis, frame, or dictionary  $\{\psi_k\}$ , meaning only a few nonzero coefficients. To enforce the sparsity of the reconstructed  $\delta\sigma$ , an  $\ell^1$  penalty is employed [Daubechies et al., 2004]

$$J_\alpha(\sigma) = \psi(\sigma) + \alpha \|\delta\sigma\|_{\ell^1}, \quad (16)$$

with

$$\psi(\sigma) = \frac{1}{2} \|F(\sigma)\mathbf{I} - \mathbf{U}^\delta\|_2^2 \quad \text{and} \quad \|\delta\sigma\|_{\ell^1} = \sum_k |\langle \delta\sigma, \psi_k \rangle|.$$

Provided that the dictionary  $\{\psi_k\}$  satisfies suitable regularity conditions, the minimization of  $J_\alpha$  over the admissible set  $\mathcal{A}$  is well-posed [Jin and Maass, 2012]. The sparsity method was first developed by Jin et al. [2012] for the continuum model, and then was later adapted to the CEM by Gehre et al. [2012] and we follow their derivation.

Optimization problems involving the  $\ell^1$  penalty have attracted intensive interest in the last two decades [Bonesky et al., 2007, Bredies et al., 2009, Daubechies et al., 2004, Wright et al., 2009]. The primary computational challenges stem from the non-differentiable nature of the  $\ell^1$  penalty coupled with the strongly nonlinearity of the term  $\psi(\sigma)$ . A basic scheme for iteratively updating  $\delta\sigma_i$  and  $\sigma_i = \sigma_0 + \delta\sigma_i$  to minimize  $J_\alpha$  is formally given by

$$\delta\sigma_{i+1} = \mathcal{S}_{s\alpha}(\delta\sigma_i - sF'(\sigma_i)^*(F(\sigma_i)\mathbf{I} - \mathbf{U}^\delta)),$$

where  $s > 0$  is the step size,  $F'(\sigma_i)$  denotes the Gâteaux derivative of the map  $F(\sigma)$  in  $\sigma$  at  $\sigma = \sigma_i$ ,  $F'(\sigma_i)^*$  denotes the adjoint of  $F'(\sigma_i)$ , and  $\mathcal{S}_\lambda(t) = \text{sign}(t) \max(|t| - \lambda, 0)$  is the soft shrinkage operator. However, the direct application of the algorithm often fails to produce satisfactory reconstructions. Instead, we implement the procedure detailed in Algorithm 1, which includes two crucial steps: the computation of the gradient  $\psi'_s$  (executed in Steps 4-5) and an appropriate step size selection (handled in Step 6).

**Gradient evaluation** To adapt the basic algorithm to the CEM setting, the gradient  $\psi'(\sigma)$  of the discrepancy term  $\psi(\sigma)$  must be computed. The gradient can be decomposed into the individual applied current patterns:

$$F'(\sigma_i)^*(F(\sigma_i)\mathbf{I} - \mathbf{U}^\delta) = \sum_{k=1}^K F'(\sigma_i)^*(F(\sigma_i)I^{(k)} - U^{\delta,(k)}). \quad (17)$$

**Algorithm 1:** Sparsity reconstruction for EIT.

**Input:** Background conductivity distribution  $\sigma_0$ , regularization parameter  $\alpha$   
**Result:** Reconstructed conductivity perturbation  $\delta\sigma$

---

```

1 Initialize perturbation estimate:  $\delta\sigma_0 \leftarrow 0$ ;
2 for  $i \leftarrow I, \dots, \text{do}$ 
3   Compute  $\sigma_i = \sigma_0 + \delta\sigma_i$ ;
4   Compute the gradient  $\psi'(\sigma_i)$ ;
5   Compute the  $H_0^1$ -gradient  $\psi'_s(\sigma_i)$ ;
6   Determine the step size  $s_i$ ;
7   Update inhomogeneity by  $\delta\sigma_{i+1} = \delta\sigma_i - s_i \psi'_s(\sigma_i)$ ;
8   Threshold  $\delta\sigma_{i+1}$  by  $\mathcal{S}_{s_i\alpha}(\delta\sigma_{i+1})$ ;
9   Check stopping criterion.
10 end

```

---

For each current pattern  $I^{(k)}$ , the respective gradient can be efficiently calculated via the adjoint technique. For notational simplicity we drop the superscript  $(k)$  below. The adjoint problem reads: Find  $(p, P) \in \mathbb{H}$  such that

$$\begin{cases} -\nabla \cdot (\sigma \nabla p) = 0, & \text{in } \Omega, \\ p + z_\ell \sigma \frac{\partial p}{\partial n} = P_\ell, & \text{on } e_\ell, \ell = 1, 2, \dots, L, \\ \int_{e_\ell} \sigma \frac{\partial p}{\partial n} ds = U_\ell(\sigma) - U_\ell^\delta, & \text{for } \ell = 1, 2, \dots, L, \\ \sigma \frac{\partial p}{\partial n} = 0, & \text{on } \Gamma \setminus \bigcup_{\ell=1}^L e_\ell, \end{cases} \quad (18)$$

where  $U(\sigma) = F(\sigma)I \in \mathbb{R}^L$  and  $U^\delta$  is the electrode voltage measurements. Given the adjoint state  $p$ , the gradient  $\psi'(\sigma)$  is given by

$$\psi'(\sigma) = -\nabla u(\sigma) \cdot \nabla p(\sigma).$$

Since  $\psi'(\sigma)$  is defined by the duality pairing  $\psi'(\sigma)[\lambda] = \langle \psi'(\sigma), \lambda \rangle_{L^2(\Omega)}$ , it belongs to the dual space  $(L^\infty(\Omega))'$  and may lack sufficient Sobolev regularity. To overcome this issue, we reformulate it using the  $H_0^1(\Omega)$  inner product  $\langle \cdot, \cdot \rangle_{H_0^1(\Omega)}$  by defining the Sobolev gradient  $\psi'_s(\sigma)$  such that  $\psi'(\sigma)[\lambda] = \langle \psi'_s(\sigma), \lambda \rangle_{H_0^1(\Omega)}$ . Integration by parts leads to the following elliptic boundary value problem

$$\begin{cases} -\Delta \psi'_s(\sigma) + \psi'_s(\sigma) = \psi'(\sigma), & \text{in } \Omega, \\ \psi'_s(\sigma) = 0, & \text{on } \Gamma. \end{cases} \quad (19)$$

The boundary condition explicitly encodes the assumption that the inclusions are in the interior of the domain  $\Omega$  and  $\sigma$  is constant on the boundary. The Sobolev gradient [Neuberger, 1997] is a regularized version of the  $L^2(\Omega)$  gradient, and it defines a smoother admissible set  $\mathcal{A}$  using the  $H_0^1(\Omega)$  topology. Numerically,  $\psi'_s(\sigma)$  is obtained by solving the Poisson equation (19). Using  $\psi'_s$ , we approximate  $J_\alpha$  locally as

$$\begin{aligned} J_\alpha(\sigma_0 + \delta\sigma) - J_\alpha(\sigma_0 + \delta\sigma_i) \\ \approx \langle \delta\sigma - \delta\sigma_i, \psi'_s(\sigma_i) \rangle_{H^1(\Omega)} + \frac{1}{2s_i} \|\delta\sigma - \delta\sigma_i\|_{H^1(\Omega)}^2 + \alpha \|\delta\sigma\|_{\ell^1}, \end{aligned}$$

which is equivalent to

$$\frac{1}{2s_i} \|\delta\sigma - (\delta\sigma_i - s_i \psi'_s(\sigma_i))\|_{H^1(\Omega)}^2 + \alpha \|\delta\sigma\|_{\ell^1}. \quad (20)$$

The minimizer  $\delta\sigma_{i+1}$  is given explicitly by

$$\delta\sigma_{i+1} = \mathcal{S}_{s_i\alpha}(\delta\sigma_i - s_i \psi'_s(\sigma_i)).$$

This step zeros out small coefficients, and promotes the sparsity of  $\delta\sigma$  with respect to the chosen basis  $\{\psi_k\}$ .

**Step size selection** Classical gradient-based methods, e.g., steepest descent, often suffer from slow convergence. To improve the computational efficiency, the Barzilai-Borwein method [Barzilai and Borwein, 1988] proposes to approximate the Hessian by a scalar multiple of the identity matrix in a least-squares sense

$$s_i = \arg \min_s \|s(\delta\sigma_i - \delta\sigma_{i-1}) - (\psi'_s(\sigma_i) - \psi'_s(\sigma_{i-1}))\|_{H^1(\Omega)}^2.$$

This gives rise to one popular Barzilai-Borwein rule [Dai et al., 2006]

$$s_i = \langle \delta\sigma_i - \delta\sigma_{i-1}, \psi'_s(\sigma_i) - \psi'_s(\sigma_{i-1}) \rangle_{H^1(\Omega)} / \|\delta\sigma_i - \delta\sigma_{i-1}\|_{H^1(\Omega)}^2.$$

In practice, following Wright et al. [2009], we enforce a weak monotonicity condition

$$\begin{aligned} & J_\alpha(\sigma_0 + \mathcal{S}_{s\alpha}(\delta\sigma_i - s\psi'_s(\sigma_i))) \\ & \leq \max_{i-M+1 \leq k \leq i} J_\alpha(\sigma_k) - \tau \frac{s}{2} \|\mathcal{S}_{s\alpha}(\delta\sigma_i - s\psi'_s(\sigma_i)) - \delta\sigma_i\|_{H^1(\Omega)}^2, \end{aligned} \quad (21)$$

where  $\tau$  is a small positive constant and  $M \geq 1$  is an integer. The step size  $s$  is initialized using the above rule and then reduced geometrically by a factor  $q \in (0, 1)$  until the weak monotonicity condition (21) is satisfied. The iteration is terminated when  $s_i$  falls below a threshold  $s_{\text{stop}}$  or after reaching the maximum number of iterations. In practice, one employs piecewise linear elements for approximating the state  $u$  as well as the conductivity  $\sigma$  in the sparse recovery, whereas in all other methods we employ piecewise constant basis for approximating  $\sigma$ .

### 3.3 Level set method

The level set method due to Osher and Sethian [1988] parameterizes a piecewise constant function using level sets of an auxiliary function. It is well-suited for EIT as we often deal with piecewise constant conductivities. The inverse problem is then cast as a fully nonlinear variational problem for the auxiliary function. The level set method was adapted to inverse problems by Santosa [1995/96] and in the context of EIT with TV regularization [Chung et al., 2005]. The original level set method was generalized in Chan and Tai [2004] to allow for multiple constant-value coefficients. It was successfully implemented for EIT [Alghamdi et al., 2024] for the Kuopio Tomography Challenge [Räsänen et al., 2024]. We follow Alghamdi et al. [2024], Chan and Tai [2004] for the description.

Let  $\Omega \subset \mathbb{R}^2$  be a smooth bounded domain, and the strictly positive  $\sigma \in L^\infty(\Omega)$  takes on four different conductive values  $\sigma_i$ ,  $i = 1, 2, 3, 4$ . Let  $\Omega_i \subset \Omega$  denote the region defined by  $\sigma(x) = \sigma_i$ . The level set parametrization uses two smooth auxiliary functions  $\phi_1$  and  $\phi_2$  defined on  $\Omega$  to represent the regions

$$\begin{aligned} \Omega_1 &= \{x \in \Omega : \phi_1 > 0, \phi_2 > 0\}, & \Omega_2 &= \{x \in \Omega : \phi_1 > 0, \phi_2 \leq 0\}, \\ \Omega_3 &= \{x \in \Omega : \phi_1 \leq 0, \phi_2 > 0\}, & \Omega_4 &= \{x \in \Omega : \phi_1 \leq 0, \phi_2 \leq 0\}. \end{aligned} \quad (22)$$

The conductivity  $\sigma$  is parametrized by the Heaviside function  $H$  and  $\phi_1, \phi_2$  as

$$\begin{aligned} \sigma(\phi_1, \phi_2) &= \sigma_1 H(\phi_1) H(\phi_2) + \sigma_2 H(\phi_1) (1 - H(\phi_2)) \\ &\quad + \sigma_3 (1 - H(\phi_1)) H(\phi_2) + \sigma_4 (1 - H(\phi_1)) (1 - H(\phi_2)), \end{aligned} \quad (23)$$

The approach allows four different conductivity values, but in the experiment we only segregate the domain  $\Omega$  into three regions, i.e., the background, higher and lower conductivity. The specific values of  $\sigma_i$  are fixed, e.g., estimated by prior knowledge, and hence the method is more qualitative than quantitative.

In the level set method, we cast the reconstruction task via the nonlinear functional

$$J(\phi_1, \phi_2) = \frac{1}{2} \| (F(\sigma(\phi_1, \phi_2)) - F(\sigma_0)) \mathbf{I} - (\mathbf{U}^\delta - \mathbf{U}_0^\delta) \|_2^2 + \alpha |\sigma(\phi_1, \phi_2)|_{\text{TV}}, \quad (24)$$

where the regularization parameter  $\alpha > 0$  can be chosen using the validation data [Chan and Tai, 2004],  $|\cdot|_{\text{TV}}$  denotes the total variation seminorm, and  $\sigma_0$  is the homogeneous background conductivity. We use the full nonlinear forward model  $F$  rather than a linearization, and the difference data rather than absolute data. To minimize the objective  $J(\phi_1, \phi_2)$ , we employ a gradient-descent method. The chain rule yields

$$\frac{\partial F}{\partial \phi_i} = F'(\sigma) \frac{\partial \sigma}{\partial \phi_i}, \quad i = 1, 2,$$

where  $F'(\sigma)$  is defined above, and formally

$$\begin{aligned} \frac{\partial \sigma}{\partial \phi_1} &= \delta(\phi_1) [\sigma_1 H(\phi_2) + \sigma_2 (1 - H(\phi_2)) - \sigma_3 H(\phi_2) - \sigma_4 (1 - H(\phi_2))], \\ \frac{\partial \sigma}{\partial \phi_2} &= \delta(\phi_2) [\sigma_1 H(\phi_1) - \sigma_2 H(\phi_1) + \sigma_3 (1 - H(\phi_1)) - \sigma_4 (1 - H(\phi_1))], \end{aligned}$$

where  $\delta$  is the Dirac delta distribution. In order to avoid dealing with such singular functions numerically, we use smooth approximations of these two functions:

$$\delta_\varepsilon(s) = \frac{\varepsilon}{\pi(s^2 + \varepsilon^2)} \quad \text{and} \quad H_\varepsilon(s) = \frac{1}{\pi} \tan^{-1} \left( \frac{s}{\varepsilon} \right) + \frac{1}{2},$$

where the small parameter  $\varepsilon > 0$  controls the smoothness; in practice we choose  $\varepsilon$  according to the mesh size  $h$ . The update in the  $j + 1$ 'th iteration is then given by

$$\phi_i^{(j+1)} = \phi_i^{(j)} - \tau \frac{dJ}{d\phi_i^{(j)}}, \quad i = 1, 2,$$

for a step length  $\tau > 0$ . The computational details including parameter choices follow Alghamdi et al. [2024]. Note that the implementation uses re-initialization of the level set functions  $\phi_i$  in order to keep them as signed distance functions. Moreover, the TV-functional is approximated smoothly and implemented via lagged diffusivity [Vogel and Oman, 1996, Adesokan et al., 2019]. Further, a good initial guess for the level set method is required to reduce the risk of trapping into local minima. For the results below we use a segmented reconstruction based on a basic linearized method like (11).

For the numerical experiments below, we choose  $\sigma_2 = 5$  and  $\sigma_3 = 0.1$ . These choices are somewhat arbitrary. In the functional  $J(\phi_1, \phi_2)$ ,  $\alpha = 5e-8$  is fixed for all experiments. Moreover, for all reconstructions, the algorithm terminates after 1000 iterations. Our implementation of the level set method uses the numerical algorithm by Alghamdi et al. [2024]. The code was developed for 32-electrode data, so the 16-electrode data used in this study require a preprocessing step. In this adaption we introduce a minor modeling error that we do not handle explicitly.

### 3.4 Direct reconstruction methods

In this part, we describe several direct methods for EIT imaging, which are specifically developed for concrete inverse problems, and essentially exploit the structure of the direct problems. The common advantage of these methods is that they are computationally efficient, and do not require the repeated application of the forward operator. However, unfortunately they also directly inherit the exponential instability to noise, hence need stabilization, generally provide reconstructions that tend to be overly smooth, and moreover, it is often challenging to include further prior knowledge into the reconstruction in the form of additional regularization. Nevertheless, direct methods can provide a proven convergent regularization, as it is the case for the D-bar algorithm [Knudsen et al., 2009]. Below we describe three direct methods, i.e., D-bar method [Siltanen et al., 2000], factorization method [Hanke and Brühl, 2003] and direct sampling method [Chow et al., 2014]. There are other direct reconstruction methods, e.g., classic Calderón's method [Bikowski and Mueller, 2008, Shin and Mueller, 2020], enclosure method [Ikehata, 1998] (with its recent learned variation [Sippola et al., 2025]), and the monotonicity method [Harrach and Ullrich, 2013].

#### 3.4.1 D-bar method

The D-bar method as implemented by Siltanen et al. [2000] relies on a reformulation of the conductivity equation into a Schrödinger-type equation and uses tools from complex scattering theory. It is based on the theoretical uniqueness proof and reconstruction algorithm by Nachman [1996]; see also later developments [Knudsen and Tamasan, 2005, Astala and Päiväranta, 2006] and the three-dimensional counterpart [Nachman, 1988, Novikov, 1988, Delbary and Knudsen, 2014, Knudsen and Rasmussen, 2022]. The method was adapted to piecewise constant conductivities by Knudsen et al. [2007].

The algorithm relies on the knowledge of the full Dirichlet-to-Neumann (DtN) map  $\Lambda_{\sigma,D}$  for the continuum model (1), which can be obtained as the inverse of the measured NtD map  $\Lambda_{\sigma,N}$ . In order to apply the algorithm to the CEM in (3), we need to transform the measurements into a representation of the DtN map  $\Lambda_{\sigma,D}$ . Note that the DtN map  $\Lambda_{\sigma,D}$  is usually represented with respect to an orthonormal basis, most commonly spherical harmonics or a trigonometric cosine/sine basis for real-valued injections. Nevertheless, in practice pairwise injections are collected for most systems, which is the case for the KIT4 system [Kourunen et al., 2008] described in Section 5. Thus, first one has to transform pairwise injections and measurements, by change of basis, into the trigonometric basis to represent the NtD-map  $\Lambda_{\sigma,N}$ . The corresponding current patterns (and basis)  $I^{(k)} \in \mathbb{R}^L$  for  $L$  and  $k = 1, \dots, L - 1$  are given by

$$I_l^{(k)} = \begin{cases} \cos((k+1)\theta_l/2), & \text{for odd } k, \\ \sin(k\theta_l/2), & \text{for even } k. \end{cases} \quad (25)$$

The estimated NtD map  $\Lambda_{\sigma,N}$  is then used to approximate the continuum data [Hyvönen, 2009, Hauptmann, 2017], and by inversion we obtain the DtN map  $\Lambda_{\sigma,D}$  needed for the D-bar method. Below we outline the classic D-bar method for  $\sigma \in C^2(\Omega)$ , with  $\sigma \geq c > 0$  in  $\Omega$ , and  $\sigma \equiv 1$  in the neighbourhood of the boundary  $\Gamma$ . Consider the embedding of  $\mathbb{R}^2$  in the complex plane, and identifying a planar point  $x = (x_1, x_2)$  with the complex number  $x_1 + ix_2$ , and the product  $kx$  denotes complex multiplication. See the survey by Mueller and Siltanen [2020] for further details.

First, the conductivity equation (1) is transformed into a Schrödinger-type equation by substituting  $\tilde{u} = \sqrt{\sigma}u$ , setting  $q = \Delta\sqrt{\sigma}/\sqrt{\sigma}$ , and extending  $\sigma \equiv 1$  outside  $\Omega$ . Then we obtain

$$(-\Delta + q(x))\tilde{u}(x) = 0, \quad \text{in } \mathbb{R}^2. \quad (26)$$

Next, we define a class of special solutions of (26) due to Faddeev [1966], i.e., complex geometrical optics (CGO) solutions  $\varphi(x, k)$ , which depend on a complex parameter  $k \in \mathbb{C} \setminus \{0\}$  and  $x \in \mathbb{R}^2$ . These exponentially behaving functions are key to the reconstruction. Specifically, given  $q \in L^p(\mathbb{R}^2)$ ,  $1 < p < 2$ , the CGO solutions  $\varphi(x, k)$  are defined to be the solutions to

$$(-\Delta + q(x))\varphi(\cdot, k) = 0, \quad \text{in } \mathbb{R}^2,$$

satisfying the asymptotic condition  $e^{-ikx}\varphi(x, k) - 1 \in W^{1, \tilde{p}}(\mathbb{R}^2)$  with  $2 < \tilde{p} < \infty$ . These solutions are unique for  $k \in \mathbb{C} \setminus \{0\}$  [Nachman, 1996, Theorem 1.1]. The D-bar method recovers the conductivity  $\sigma$  from the knowledge of the CGO solutions  $\mu(x, k) = e^{-ikx}\varphi(x, k)$  at the limit  $k \rightarrow 0$  [Nachman, 1996, Section 3]

$$\lim_{k \rightarrow 0} \mu(x, k) = \sqrt{\sigma}, \quad x \in \Omega.$$

Numerically, one can substitute the limit by  $k = 0$  and evaluate  $\mu(x, 0)$ . The reconstruction of  $\sigma$  uses an intermediate object called the (non-physical) scattering transform  $\mathbf{t}$ , defined by

$$\mathbf{t}(k) = \int_{\mathbb{R}^2} e_k(x) \mu(x, k) q(x) dx,$$

with  $e_k(x) := \exp(i(kx + \bar{k}\bar{x}))$ , where over-bar denotes complex conjugate. Since  $\mu$  is asymptotically close to one,  $\mathbf{t}(k)$  is similar to the Fourier transform of  $q(x)$ . We obtain  $\mu$  by solving the name-giving D-bar equation

$$\bar{\partial}_k \mu(x, k) = \frac{1}{4\pi k} \mathbf{t}(k) e_{-k}(x) \overline{\mu(x, k)}, \quad k \neq 0, \quad (27)$$

where  $\bar{\partial}_k = \frac{1}{2}(\frac{\partial}{\partial k_1} + i\frac{\partial}{\partial k_2})$  is known as the D-bar operator. To solve (27), the scattering transform  $\mathbf{t}(k)$  is required, which we cannot measure directly in the experiment, but  $\mathbf{t}(k)$  can be represented using the DtN map  $\Lambda_{\sigma, D}$ . Indeed, using Alessandrini's identity [Alessandrini, 1988], we get

$$\mathbf{t}(k) = \int_{\Gamma} e^{i\bar{k}\bar{x}} (\Lambda_{\sigma, D} - \Lambda_{1, D}) \varphi(x, k) ds. \quad (28)$$

Note that  $\Lambda_{1, D}$  can be analytically computed, and only  $\Lambda_{\sigma, D}$  needs to be obtained from the measurement. One can either compute the scattering transform  $\mathbf{t}(k)$  using a Born approximation  $\varphi \approx e^{ikx}$ , leading to a linearized approximation, or solve a Fredholm boundary integral equation of the second kind using Faddeev's Green's function as well as the measured difference operator  $\Lambda_{\sigma, D} - \Lambda_{1, D}$  [Nachman, 1996]. In the numerical experiments, we employ the full nonlinear algorithm.

The resulting D-bar algorithm is highly parallelizable in each step. First, the computation of the CGO solutions  $\varphi(x, k)$  and  $\mathbf{t}(k)$  are both independent of  $k$ . Second, the solutions of (27) are also independent for each  $x \in \Omega$  and one can efficiently parallelize over  $x$ . This leads to real-time implementations [Dodd and Mueller, 2014], which is especially relevant for time-critical applications, e.g., monitoring purposes.

Note that the algorithm assumes infinite precision and exact data. When the measured data is noisy and comes from a finite number of electrode measurements, the resulting DtN map  $\Lambda_{\sigma, D}$  is inaccurate, and the computation of  $\mathbf{t}(k)$  becomes exponentially unstable for  $|k| > R$  for some radius  $R$ . Thus, in practice, we restrict the computation to a certain frequency range in order to stably compute  $\mathbf{t}(k)$ . We choose  $R = 4$  throughout this study. The overall procedure is summarized in Algorithm 2.

---

**Algorithm 2:** D-bar algorithm using  $\mathbf{t}^{\text{exp}}$ 


---

**Input:**  $\Lambda_{\sigma, D}$  and  $R$

**Result:** Regularised reconstruction of  $\sigma$

- 1 Compute analytic  $\Lambda_{1, D}$ ;
  - 2 Obtain  $\varphi(x, k)$  for  $|k| < R$  from boundary integral equation;
  - 3 Evaluate  $\mathbf{t}(k)$  for  $|k| < R$  by (28);
  - 4 Solve the D-bar equation (27);
  - 5 Obtain  $\sigma(x) = \mu(x, 0)^2$  for  $x \in \Omega$ ;
- 

### 3.4.2 Sampling methods

Sampling methods are a class of qualitative methods in which a set of test points is selected to determine whether each point belongs to the inclusion support. Specifically, the unknown  $\sigma: \Omega \rightarrow \mathbb{R}$  consists of a known constant background  $\sigma_0$  and unknown inclusions, modeled as a subset  $D \subset \Omega$ . In a sampling method, one constructs an indicator function to

indicate for each test point  $x \in \Omega$ , whether it lies within  $D$ . These methods are typically tailored to the structure and properties of the specific inverse problem, and include linear sampling method [Kirsch, 1998, Cheney, 2001, Somersalo, 2001], Multiple Signal Classification [Cheney, 2001, Lechleiter, 2015], and direct sampling method [Ito et al., 2012, Chow et al., 2014, Ito et al., 2025]. All of them were initially developed for inverse scattering problems and then adapted to EIT.

**Factorization method** The factorization method due to Hanke and Brühl [2003] is one classical sampling technique for the continuum model (1) of EIT. In the method, one factorizes the difference between the NtD operators of the true conductivity  $\sigma$  and the background  $\sigma_0$ , and constructs a function  $h_z$  for each point  $z \in \Omega$ . Then  $z$  lies within the inclusion  $D$  if and only if  $h_z$  belongs to the range of the operator  $(\Lambda_{\sigma,N} - \Lambda_{\sigma_0,N})^{1/2}$ . By the Picard criterion, we deduce

$$z \in D \iff \sum_{n=0}^{\infty} \frac{\langle h_z, v_n \rangle^2}{\lambda_n} < \infty,$$

where  $(\lambda_n)$  and  $(v_n)$  are the eigenvalues and eigenfunctions of the difference operator  $\Lambda_{\sigma,N} - \Lambda_{\sigma_0,N}$ , respectively.

**Direct sampling method** The direct sampling method (DSM) [Chow et al., 2014] is also well-known for identifying conductivity anomalies using the continuum model (1). Using only one single pair of Cauchy data on the boundary  $\Gamma$ , the DSM constructs a family of probing functions  $\{\eta_{x,d_x}\}_{x \in \Omega, d_x \in \mathbb{R}^d} \subset H^{2\gamma}(\Gamma)$ , for some  $\gamma \geq 0$ , and defines an index function

$$\mathcal{I}(x, d_x) := \frac{\langle \eta_{x,d_x}, u_\sigma - u_{\sigma_0} \rangle_{\gamma, \Gamma}}{\|u_\sigma - u_{\sigma_0}\|_{L^2(\Gamma)} |\eta_{x,d_x}|_Y}, \quad x \in \Omega,$$

where  $u_\sigma$  and  $u_{\sigma_0}$  are the solutions of problem (1) for  $\sigma$  and  $\sigma_0$ , respectively, both with the current  $j$ . The notation  $|\cdot|_Y$  denotes the  $H^{2\gamma}(\Gamma)$  seminorm and the duality product  $\langle f, g \rangle_{\gamma, \Gamma}$  is defined by

$$\langle f, g \rangle_{\gamma, \Gamma} = \int_{\Gamma} (-\Delta_{\Gamma})^\gamma f g ds = \langle (-\Delta_{\Gamma})^\gamma f, g \rangle_{L^2(\Gamma)},$$

where  $-\Delta_{\Gamma}$  denotes the Laplace-Beltrami operator, and  $(-\Delta_{\Gamma})^\gamma$  its fractional power defined via spectral calculus. More precisely, let the Cauchy difference function  $\varphi$  be defined by the solution of

$$\begin{cases} -\Delta \varphi = 0, & \text{in } \Omega, \\ \frac{\partial \varphi}{\partial n} = (-\Delta_{\Gamma})^\gamma (u_\sigma - u_{\sigma_0}), & \text{on } \Gamma, \\ \int_{\Gamma} \varphi ds = 0, & \end{cases} \quad (29)$$

i.e., the EIT forward problem for the background conductivity with the applied current  $j$  replaced by  $u_\sigma - u_{\sigma_0}$ . Then the index function  $\mathcal{I}(x, d_x)$  is given by

$$\mathcal{I}(x, d_x) := \frac{d_x \cdot \nabla \varphi(x)}{\|\phi_\sigma - \phi_{\sigma_0}\|_{L^2(\Gamma)} |\eta_{x,d_x}|_Y}, \quad x \in \Omega.$$

The unit vector  $d_x = \nabla \varphi(x) / \|\nabla \varphi(x)\|_{L^2(\Gamma)}$  was chosen to carry out the numerical experiments by Chow et al. [2014] to prevent the direction  $d_x$  from being orthogonal to  $\nabla \varphi(x)$  and accidentally removing existing inclusions.

Ideally the index function  $\mathcal{I}(x, d_x)$  should assume large values at points near / inside the inclusions and relatively small values for points far away from  $D$ . This relies heavily on the choice of the Sobolev dual product  $\langle \cdot, \cdot \rangle_{\gamma, \Gamma}$ . Very recently, this approach was extended by Ito et al. [2025], by incorporating an iterative mechanism, so as to achieve better resolution and numerical stability. However, these developments are for the continuum model (1). Below we propose a deep learning version of the DSM for the CEM.

## 4 Learned reconstruction methods

The development of deep learning techniques has significantly advanced EIT reconstruction in recent years. Deep neural networks (DNNs) address the ill-posed nature of EIT by choosing specific network architectures and by learning nonlinear mappings between input data and reconstruction outputs. Recent studies demonstrate notable improvements in key metrics, e.g., noise robustness, structural fidelity, and resolution enhancement, thereby significantly broadening EIT's applicability in biomedical diagnostics and nondestructive testing. The aim of learned methods is to replace parts

or even the entire reconstruction process by DNNs trained on available (paired) training data. These methods differ in the parts that are replaced by DNNs, and how the DNNs are trained.

All deep learning approaches discussed in this study utilize convolutional neural networks (CNNs), which are particularly well-suited for pixel-based image data. However, in EIT, the forward operator is discretized using FEM meshes, which are typically composed of triangular elements. This mesh-based representation is incompatible with CNNs, necessitating an interpolation step to transform the mesh data into a pixel-grid format. Herzberg et al. [2021, 2023] and Toivanen et al. [2025] address this limitation using graph convolutional networks to process mesh-based data directly, eliminating the need for interpolation. Additionally, domain-adapted network architectures, e.g., neural operators [Azizzadenesheli et al., 2024], offer a promising research avenue by learning mappings between function spaces, enabling efficient handling of data on irregular or mesh-based domains.

In the following we survey different supervised and unsupervised learned reconstruction methods, and the specific approaches used in the comparative study. Roughly these approaches can be grouped into

- Fully learned approaches
- Post-processing methods
- Deep direct sampling method
- Learned iterative methods
- Unsupervised methods

Recently, also deep generative models have been applied to EIT; see the review by Wang et al. [2024]. For example, Alberti et al. [2024] learn a mixture of variational autoencoders [Kingma and Welling, 2014] to approximate the data manifold. Also, Seo et al. [2019] propose to use variational autoencoders and to exploit the low dimensional latent space for lung EIT. Denker et al. [2024] employ score-based models [Song et al., 2021] to model the posterior distribution. However, these methods are not included in the study.

#### 4.1 Fully-learned approaches

In the existing literature, a substantial body of research focuses on fully-learned approaches by designing DNN architectures  $\mathcal{R}_\theta$  that directly approximate the inverse mapping from boundary voltage measurements  $\mathbf{U}^\delta$  to the conductivity distributions  $\sigma$ , such that  $\sigma \approx \mathcal{R}_\theta(\mathbf{U}^\delta)$ , based on supervised learning over paired training datasets. Early approaches by Adler and Guardo [1994] employ a single linear layer to learn the relationship between the mapping and conductivity. Li et al. [2017] proposed a four-layer architecture built upon stacked autoencoders and a logistic regression layer. Tan et al. [2018] followed with a convolutional model inspired by LeNet, incorporating pooling and dropout layers to enhance the robustness. More recent developments include hybrid designs such as the FC-UNet proposed by Chen et al. [2020], which first uses a fully connected layer to convert voltage data into image features before applying a UNet for final reconstruction. Yang et al. [2023] introduced a DenseNet model featuring multiscale convolution to further capture fine conductivity structures. Compact and low-rank-aware architectures have been proposed by Fan and Ying [2020], targeting both forward and inverse problems in 2D and 3D. Huang et al. [2019] combine radial basis function models for initial estimates with UNet-based refinement. Meanwhile, variational autoencoder-based approaches, see e.g. Seo et al. [2019], explore latent space representations of the conductivity to facilitate dimensionality reduction.

One prototypical example of a fully-learned approach is the FC-UNet [Chen et al., 2020]. We implement a variation of the method in the experimental evaluation. The FC-UNet directly learns a mapping from the measurements to reconstructions with a linear fully connected layer and a UNet [Ronneberger et al., 2015a], eliminating the need for any physical modeling. We parametrize the reconstruction operator  $\mathcal{R}_\theta$  as

$$\mathcal{R}_\theta(\mathbf{U}^\delta) := \mathcal{G}_\theta(\mathcal{S}(\mathbf{W}\mathbf{U}^\delta)),$$

where  $\mathbf{W}$  is a learnable matrix, mapping the measurements to an initial image, and  $\mathcal{G}_\theta$  is implemented as a UNet. The parameter count of the initial matrix  $\mathbf{W}$  grows quadratic with the image resolution. For example, with a resolution  $N = 128$  and the KIT4 setting ( $K = 76$  and  $L = 16$ ) the matrix  $\mathbf{W} \in \mathbb{R}^{128^2 \times KL}$  already has about 20M parameters. The high parameter count poses major computational and memory challenges during training. To partially address these challenges, we use a smaller initial image resolution ( $N = 64$ ), followed by a bilinear upsampling  $\mathcal{S} : \mathbb{R}^{64^2} \rightarrow \mathbb{R}^{256^2}$  to match the target resolution of the UNet. In the original implementation of the FC-UNet [Chen et al., 2020] the authors use the ReLU after the initial linear layer to constrain the input to the UNet to be nonnegative. In our experiments, we find that this additional operation is not necessary and we remove it for simplicity.

We employ a two-step approach to train the FC-UNet. First, by initializing the matrix  $\mathbf{W}$  to zero, we train it via the mean squared error loss

$$\min_{\mathbf{W}} \sum_{i=1}^n \|\mathcal{S}(\mathbf{W}\mathbf{U}^{\delta,(i)}) - \sigma^{(i)}\|_2^2. \quad (30)$$

This training procedure estimates an optimal linear reconstruction operator  $\mathbf{W}$  with respect to the least-squares loss. After pre-training the matrix  $\mathbf{W}$ , we train the entire network (including  $\mathbf{W}$ ) by minimizing

$$\min_{\mathbf{W}, \theta} \sum_{i=1}^n \|\mathcal{G}_\theta(\mathcal{S}(\mathbf{W}\mathbf{U}^{\delta,(i)})) - \sigma^{(i)}\|_2^2. \quad (31)$$

We use a total of 110 epochs, with 10 epochs for the pre-training of  $\mathbf{W}$  and 100 epochs for the full network. The UNet has an input resolution of 256 and employs 4 downsampling steps. We use attention layers at resolution 32 and 16 following Dhariwal and Nichol [2021]. The total network has 11 486 625 parameters, where 4 980 736 are used by the initial linear layer. We employ the Adam optimizer [Kingma and Ba, 2015] with a cosine annealing learning rate, starting at  $1e-4$  and reducing to  $1e-7$  with a batch size of 32. For the final evaluation we pick the model with the lowest validation loss.

## 4.2 Post-processing methods

To leverage the stability and interpretability of analytic methods, many recent studies have explored hybrid strategies based on post-processing where trained neural networks are employed to refine or enhance results from model-based reconstructions. Formally, these methods learn  $\sigma \approx \mathcal{G}_\theta(\mathcal{R}(\mathbf{U}^\delta))$ , where  $\mathcal{R}$  is a classical (non-learned) reconstruction operator. One prominent example is the Deep D-bar method [Hamilton and Hauptmann, 2018], which employs the D-bar method for the initial image reconstruction followed by a UNet for enhancement. Extensions of this strategy include deep versions of Calderón’s method [Cen et al., 2023, Sun et al., 2023, Li et al., 2025], the domain-current method [Wei et al., 2019], iterative solvers like Gauss-Newton [Martin and Choi, 2017] and conjugate gradient [Zhang et al., 2022] and multi-scale frequency enhanced deep D-bar method Cao et al. [2025]. The Deep DSM (DDSM) due to Guo and Jiang [2021] is a further innovation different from post-processing, leveraging Cauchy difference functions (instead of approximations to the inclusions) derived from the direct sampling method as inputs to a CNN.

We implement two post-processing approaches: the deep D-bar method and linearized post-processing. These methods share the neural network architecture for refinement but differ in the choice of the initial reconstruction. We use the same UNet architecture as for the FC-UNet, including attention layers and a total parameter count of 6 305 185

In the deep D-bar method [Hamilton and Hauptmann, 2018], we first obtain a stable regularized reconstruction using the D-bar method, denoted by  $\mathcal{R}_{\bar{\partial}}$  (see Algorithm 2). This step maps the measured DtN-map  $\Lambda_{1,D}^{(i)}$  for sample  $i$  to an approximate reconstruction, i.e.,  $\sigma^{(i)} \approx \mathcal{R}_{\bar{\partial}}(\Lambda_{1,D}^{(i)})$ . The UNet reconstructs the pixel values on a rectangular grid. One distinct strength of the D-bar method in the context is that the reconstructions can be computed for any  $x \in \Omega$  (even for any  $x \in \mathbb{R}^2$ ). Hamilton et al. [2019] extended this capability to train domain-shape-independent networks. Initially, the D-bar reconstructions are generated on the  $[-1, 1]^2$  pixel grid with  $128^2$  pixels. Even though some points on this grid lie outside the measurement domain, the reconstructions at these points can contain valuable information, enhancing the post-processing stage.

In the linearized post-processing method, the input to the UNet  $\mathcal{G}_\theta$  is the linearized reconstruction  $\widehat{\delta\sigma}$ , cf. (15). Since the linearized reconstruction is defined on a mesh while the UNet operates on a pixel grid, a linear interpolation step is incorporated to map the reconstruction onto the pixel grid.

Given the initial reconstruction  $\sigma_{\text{reco}}$ , either given by  $\mathcal{R}_{\bar{\partial}}(\Lambda_{1,D})$  or  $\widehat{\delta\sigma}$ , the CNN is trained to minimize the mean squared error over the paired training data  $\{(\sigma_{\text{reco}}^{(i)}, \sigma^{(i)})\}$ :

$$\min_{\theta} \sum_{i=1}^n \|\mathcal{G}_\theta(\sigma_{\text{reco}}^{(i)}) - \sigma^{(i)}\|_2^2, \quad (32)$$

to match the ground truth conductivity distribution. To minimize the loss, we employ the Adam optimizer [Kingma and Ba, 2015]. We train the model for 200 epochs with a cosine learning rate decay with an initial learning rate of  $1e-4$ , decreasing to a final learning rate of  $1e-5$ . The model selected for final evaluation is the one achieving the lowest mean squared error on the validation set. Note that once the DNN  $\mathcal{G}_\theta$  is trained, for each test data  $\Lambda_{\sigma,D}^*$ , deploying the method requires only feeding the initial reconstruction through the neural network, which is computationally very efficient.

### 4.3 Deep direct sampling method

Inspired by the direct sampling method (DSM) [Chow et al., 2014], Guo and Jiang [2021] proposed the Deep Direct Sampling Method (DDSM), which employs multiple pairs of Cauchy data to train a CNN-based UNet network [Ronneberger et al., 2015b] to learn a relationship between the Cauchy difference functions  $\varphi_i$  and the true inclusion distribution. More specifically, the DDSM constructs and trains a UNet  $\mathcal{G}_\theta$  such that

$$\sigma \approx \mathcal{G}_\theta(\varphi_1, \varphi_2, \dots, \varphi_N), \quad (33)$$

where  $\{\varphi_i\}_{i=1}^N$  correspond to  $N$  pairs of Cauchy data  $\{j_\ell, \Lambda_{\sigma, N} j_\ell\}_{\ell=1}^N$ , see (29). The following theorem [Guo and Jiang, 2021, Theorem 4.1] provides the mathematical foundation for the DDSM.

**Theorem 4.1.** *Let  $\{j_\ell\}_{\ell=1}^\infty$  be a fixed orthonormal basis of  $H^{-1/2}(\Gamma)$ . Given an arbitrary  $\sigma$  such that  $\sigma > \sigma_0$  or  $\sigma < \sigma_0$ , let  $\{j_\ell, \Lambda_{\sigma, N} j_\ell\}_{\ell=1}^\infty$  be the Cauchy data pairs and let  $\{\varphi_\ell\}_{\ell=1}^\infty$  be the corresponding Cauchy difference functions. Then the inclusion distribution  $\sigma$  can be uniquely determined from  $\{\varphi_\ell\}_{\ell=1}^\infty$ .*

The idea of the DDSM has been further extended to a transformer-based approach by Guo et al. [2023], using the harmonic extension as different input channels, which is inspired by the DSM. The authors employed learnable non-local kernels, in which direct sampling is recast to a modified attention mechanism.

To the best of our knowledge, the (D)DSM for the CEM has not been studied so far. Motivated by the method developed by Guo and Jiang [2021], we propose a version of the DDSM for the CEM by training a UNet network, as in (33), to learn the relationship between the Cauchy difference functions  $\{\varphi_i\}_{i=1}^L$  and the sought-after conductivity  $\sigma$ . More precisely, in the CEM version of the DDSM, each function  $\varphi_i$  corresponds to the first entry of the pair  $(\varphi_i, V) \in H^1(\Omega) \oplus \mathbb{R}_\circ^L$ , which is the solution of the following PDE

$$\begin{cases} -\Delta \varphi_i = 0, & \text{in } \Omega, \\ \varphi_i + z_\ell \frac{\partial \varphi_i}{\partial n} = V_\ell, & \text{on } e_\ell, \ell = 1, 2, \dots, L, \\ \int_{e_\ell} \frac{\partial \varphi_i}{\partial n} ds = (U_\sigma^{\delta, (i)} - U_{\sigma_0}^{(i)})_\ell, & \ell = 1, 2, \dots, L, \\ \frac{\partial \varphi_i}{\partial n} = 0, & \text{on } \Gamma \setminus \cup_{\ell=1}^L e_\ell, \end{cases}$$

with  $V = (V_1, \dots, V_L)$ . In addition,  $U_\sigma^{\delta, (i)}, U_{\sigma_0}^{(i)} \in \mathbb{R}^L$  are the (measured) potentials at the electrodes for the conductivity  $\sigma$  and the background  $\sigma_0$ , respectively. Note that similarly to the method of Guo and Jiang, the function  $\varphi_i$  corresponds to (part of) the solution of the PDE that models the forward problem of EIT, with the background constant conductivity, and with the current pattern replaced by the difference  $U_\sigma^{\delta, (i)} - U_{\sigma_0}^{(i)}$ , see (29) and (3). Formally it lifts the electrode voltage difference to the domain  $\Omega$ .

The final model is based on the UNet architecture with an input and output resolution of  $64 \times 64$  px. The model has 16 input channels, one for each (discretised) difference function  $\{\varphi_i\}_{i=1}^L$ . It has 24 006 273 trainable parameters.

### 4.4 Learned iterative methods

One prominent class of hybrid methods relies on unrolling iterative solvers into DNNs. These architectures learn parameterized update rules by mimicking optimization procedures such as ADMM or Gauss-Newton iterations. Originally, learned iterative methods were proposed for image reconstruction in linear inverse problems, with notable applications in MRI and CT [Adler and Öktem, 2017, 2018, Hammerl et al., 2018]. Extensions to EIT include the MMV-Net [Chen et al., 2023], which unfolds ADMM steps for multi-frequency EIT, and unrolled Gauss-Newton method (Herzberg et al. [2021] and Colibazzi et al. [2023] for learning Gauss-Newton updates and proximal operators, respectively). Quasi-Newton updates via learned SVD approximations have also been proposed [Smyl et al., 2021]. Alberti et al. [2025] unroll the iterative proximal regularized Gauss-Newton method with graph neural networks (GNNs) for multi-frequency EIT. These approaches offer a balance between physical modelling and data-driven learning.

In this study we investigate the learned Gauss-Newton method: we unroll a (fixed) number of Gauss-Newton updates

$$\sigma_{k+1} := \sigma_k + \delta\sigma_k, \quad k = 1, \dots, K, \quad (34)$$

where  $\delta\sigma_k$  is given by the Gauss-Newton update step. Then, the additive update  $\delta\sigma$  is replaced with a learned update using a neural network

$$\sigma_{k+1} = \mathcal{G}_{\theta_k}(\sigma_k, \delta\sigma_k), \quad k = 1, \dots, K, \quad (35)$$

where each subnetwork has individual parameters  $\theta_k$ . Similar to Herzberg et al. [2021] we employ Gauss-Newton updates with a smoothed TV regularization, cf. (14) in Section 3.1. Since the Gauss-Newton update step is given on the FEM mesh, Herzberg et al. [2021] employ GNNs for all subnetworks  $\mathcal{G}_{\theta_k}$  to directly process the mesh representation. However, instead of employing GNNs, we utilize CNNs as in Mozumder et al. [2021], which requires additional interpolation steps both before and after applying the FEM model. The interpolation layers map the mesh to a regular grid suitable for CNNs and then map the output of the network back to the FEM domain. The full model, referred to as Deep GN-TV, is trained iteratively using a greedy training strategy [Hauptmann et al., 2018]: each subnetwork is trained iteratively, i.e., for  $k = 1, \dots, K$ , we minimize the loss

$$\min_{\theta_k} \sum_{i=1}^n \|\sigma^{(i)} - \mathcal{G}_{\theta_k}(\sigma_{k-1}^{(i)}, \delta\sigma_{k-1}^{(i)})\|_2^2, \quad (36)$$

where  $\sigma_{k-1}^{(i)}$  is the prediction from the previous subnetwork for the  $i$ -th example and  $\delta\sigma_{k-1}^{(i)}$  is the GN-TV update. After training the  $k$ -th subnetwork, all weights in the subnetwork are frozen and the next subnetwork  $k+1$  is trained. Greedy training results in iteration-wise optimality, which serves as an upper bound to end-to-end optimality. This training method separates the training of the subnetworks and the application of the FEM model, which reduces the computational complexity. Further, we do not have to back-propagate through the FEM model and through the construction of the Jacobian. In our implementation, we unroll GN-TV for 6 iterations and each subnetwork  $\mathcal{G}_{\theta_k}$  is implemented as a small UNet with 3 downsampling operations. Each subnetwork has 124 265 trainable parameters. The model has 745 590 parameters.

Learned iterative methods often achieve the best performance in practice [Arridge et al., 2019]. However, they have a significant limitation in terms of the computational cost. For each example and iteration, they require the GN-TV update step, which involves computing the Jacobian and thus substantially increases the computational complexity. In contrast, post-processing and fully-learned methods are relatively inexpensive to deploy. For example, the linearized post-processing approach requires only one single Jacobian of the constant background (which can be reused for multiple inputs), while the FC-UNet requires only a single forward pass through the DNN.

#### 4.5 Unsupervised methods

Despite their effectiveness, supervised models depend heavily on the quality, size and representativeness of the training data. Due to the challenge associated with acquiring large-scale paired training data under varied settings, most current datasets in EIT are synthetically generated. While training on simulated phantoms enables flexibility, generalization can be limited: These methods tend to perform well only when the test data closely matches the training distribution. In contrast, robustness against domain shift, geometry variations, and realistic noise remains a pressing challenge in deep learning-based image reconstruction techniques [Antun et al., 2020]. In this survey we focus on supervised learned methods, i.e., on deep learning concepts that explicitly exploit the data structure. However, there do exist various unsupervised concepts, that have been applied to the EIT problem. We will briefly review the state of research but do not include such methods in the subsequent numerical comparison.

To reduce the need of ground-truth data, several physics-driven unsupervised and weakly supervised strategies have been developed, incorporating physical constraints directly into the learning process. Physics-Informed Neural Networks [Raissi et al., 2019] represent a major milestone in this direction. Bar and Sochen [2021] proposed using DNNs to simultaneously represent the conductivity  $\sigma$  and multiple voltage potentials  $\{u_j\}$ , training the model to satisfy the governing PDE and boundary conditions in a strong form (in the continuum model). Similar approaches combine data-driven learning with energy-based models to enhance robustness and convergence [Pokkunuru et al., 2022]. One unsupervised direction is the Deep Image Prior [Ulyanov et al., 2018], applied to EIT by Liu et al. [2023], in which a CNN is trained per instance by optimizing image quality against measurement consistency, using no external data. Chen and Liu [2025] developed an approach for high-contrast EIT by combining latent surface representation and shape optimization. While being computationally intensive, these physics-driven models and their variants offer high adaptivity and robustness under distributional shift, since they do not rely on paired datasets.

## 5 Experimental setup

Due to the lack of large paired datasets for training learned reconstruction methods in EIT, we rely on simulated data. We create a dataset of simulated elliptical inclusions. This dataset is used to train the learned reconstructors and to choose the hyperparameters (e.g., regularization parameters and number of iterations) for the classical reconstruction methods. For testing, we utilize a held-out subset of these simulated ellipses and further evaluate the methods on phantoms featuring out-of-distribution inclusions, e.g., rectangles and triangles. Finally, all methods are evaluated

on real measured data from the KIT4 dataset [Hauptmann et al., 2017]. The KIT4 dataset does not provide ground-truth conductivity distribution, only photos of the watertank containing different inclusions. We make use of these photographs and create hand-annotated segmentation masks, which are then used in the evaluation routine. In this section, we first define the evaluation metrics used, and then describe the datasets and simulation setup.

### 5.1 Evaluation scores

We evaluate the reconstruction methods using a range of scores that highlight different aspects of reconstruction quality. All evaluation scores are calculated on the FEM mesh. For CNN-based network architectures, this requires an interpolation step, mapping the pixel-based image to the FEM mesh.

**Relative  $L^1/L^2$ -error** First, we use two global metrics, the *relative  $L^1$ -error* and the *relative  $L^2$ -error*, to assess the overall reconstruction accuracy. Given the ground truth conductivity distribution  $\sigma_{\text{gt}}$  and the reconstruction  $\sigma_{\text{rec}}$  and the relative  $L^1$ -error and the relative  $L^2$ -error are defined respectively by

$$\begin{aligned} \text{L1rel}(\sigma_{\text{gt}}, \sigma_{\text{rec}}) &= \frac{\int_{\Omega} |\sigma_{\text{gt}} - \sigma_{\text{rec}}| dx}{\int_{\Omega} |\sigma_{\text{gt}}| dx}, \\ \text{L2rel}(\sigma_{\text{gt}}, \sigma_{\text{rec}}) &= \frac{\int_{\Omega} (\sigma_{\text{gt}} - \sigma_{\text{rec}})^2 dx}{\int_{\Omega} \sigma_{\text{gt}}^2 dx}. \end{aligned}$$

**Dice Score** Next, we compute a task-based score, i.e., dice score, to evaluate the accuracy of the localization of inclusion, similar to Räsänen et al. [2024]. The motivation behind dice score is that while some methods may overestimate or underestimate the intensity, they may still perform well in localizing the inclusions. Using Otsu's algorithm [Otsu, 1975], the conductivity distribution is segmented into resistive and conductive inclusions and background regions. We then compute the *dice score* (DS) as the mean dice coefficient over the three classes, where the dice coefficient is defined as

$$\text{DSC} = \frac{2\text{TP}}{2\text{TP} + \text{FP} + \text{FN}}, \quad (37)$$

with true positive (TP), false positive (FN) and false negative (FN). The dice coefficient is between 0 and 1, where 1 corresponds to a perfect segmentation. Note that the Dice score may not reflect image quality accurately, due to the involved segmentation.

**Dynamic Range** To measure whether the intensity values are overestimated or underestimated by a reconstruction method, we compute the *dynamic range* (DR) [Herzberg et al., 2021] as

$$\text{DR}(\sigma_{\text{gt}}, \sigma_{\text{rec}}) = \frac{\max(\sigma_{\text{rec}}) - \min(\sigma_{\text{rec}})}{\max(\sigma_{\text{gt}}) - \min(\sigma_{\text{gt}})}. \quad (38)$$

A dynamic range of 1 means that the intensity range of the ground truth was reconstructed perfectly.

**Measurement Error** Finally, we compute the *measurement error*. It measures the error between the predicted potential at the electrodes  $\mathbf{F}(\sigma_{\text{rec}})\mathbf{I}$  and the measurements  $\mathbf{U}^\delta$ . We compute it as

$$\text{MeasErr}(\sigma_{\text{rec}}, \mathbf{U}^\delta) = \frac{\|\mathbf{F}(\sigma_{\text{rec}})\mathbf{I} - \mathbf{U}^\delta\|_2^2}{\|\mathbf{U}^\delta\|_2^2}. \quad (39)$$

The measurement error coincides with the data fitting of the reconstruction  $\sigma_{\text{rec}}$ .

### 5.2 Simulation setting

We create a synthetic dataset of conductivity distributions, following the simulation protocol described in Tanyu et al. [2025]. Each phantom contains 1 to 3 non-overlapping elliptical inclusions with a uniform background with a conductivity value 1.31, matching the KIT4 system. The conductivity values of the inclusions are sampled independently, with lower values sampled from  $\mathcal{U}[0.01, 0.3]$  and higher values sampled from  $\mathcal{U}[2.0, 3.0]$ . The dataset is divided into training (2000 pairs), validation (200 pairs), and test (100 pairs) subsets. In addition to these elliptical inclusions, we create out-of-distribution phantoms with different shapes. See Figure 1 for both in-distribution and out-of-distribution phantoms.

Measurements were simulated according to the KIT4 setup [Hauptmann et al., 2017], i.e., a circular domain with 16 equidistant electrodes covering 45% of the boundary. We utilize two meshes with triangular elements: a coarse mesh with 5248 elements, and a dense mesh with 8072 elements. For both meshes, we align the mesh points on the boundary

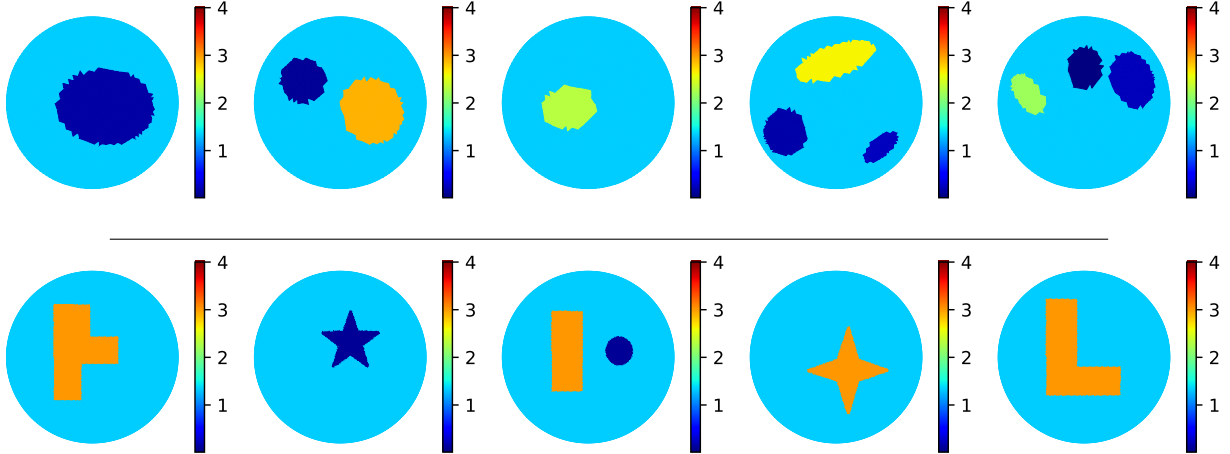


Figure 1: Exemplary ground truth phantoms of the simulated dataset. First row: In-distribution samples with elliptical inclusions. Second row: Out-of-distribution phantoms.

with the extend of the electrode, such that each electrode is perfectly covered by a fixed number of mesh elements. The dense mesh was used in the FEM solver, see Section 2.2, to simulate the measurements, whereas the coarse mesh was used to solve the inverse problem. We use piecewise constant basis functions for the conductivity  $\sigma$  and piecewise linear basis functions for the potential  $u$ . Further, we added 0.5% relative noise:

$$\mathbf{U}^\delta = \mathbf{U} + \delta \text{ mean}(|\mathbf{U}|)\epsilon, \quad \epsilon \sim \mathcal{N}(0, \mathbf{I}), \quad (40)$$

with  $\delta = 0.005$ . This noise level was chosen to achieve a similar SNR as the KIT4 experiments [Hauptmann et al., 2017].

### 5.3 The KIT dataset

The KIT4 dataset is an open dataset [Hauptmann et al., 2017] of EIT measurements from the Kuopio Impedance Tomograph 4 (KIT4) located at the University of Eastern Finland [Kourunen et al., 2008]. The measurements were taken on a circular tank of radius 14 cm with 16 electrodes of width 2.5 cm and tap water with a conductivity value 0.03 S/m filled to a height of 7 cm. Between 1 to 3 conductive (metal) and resistive (plastic) targets were placed in the tank, with a total of 22 different measurements. Adjacent current patterns with amplitude 2 mA were applied at 1 kHz. Additionally, an out-of-distribution dataset has been collected comprising a resistive foam close to the boundary  $\Gamma$  with inclusions inside (13 measurements), as well as one final measurements of a pumpkin.

The KIT4 dataset lacks ground truth conductivity distributions, making it impossible to compute the evaluation scores outlined in Section 5.1, with the exception of the measurement error. However, the dataset includes photographs of the watertank with various inclusions. These images were manually annotated to create segmentation masks, categorizing regions into resistive/conductive inclusions and background. These annotated masks were used to calculate the Dice Score, allowing a quantitative comparison of the reconstruction methods.

## 6 Numerical results

In this section we evaluate the model-based and learned reconstruction methods on three distinct datasets: the held-out test set of simulated ellipses, a small simulated dataset of differently shaped inclusions and the KIT4 dataset. In particular, we evaluate the linearized reconstruction method (**Lin-Rec**, see (15)), **D-Bar** (see Section 3.4.1), sparsity reconstruction (**L1-Sparsity**, see Section 3.2), Gauss-Newton TV (**GN-TV**, see (14)), **FC-UNet** (see Section 4.1), post-processing UNet (**Post-UNet**, see Section 4.2), **Deep D-bar** (see Section 4.2), deep direct sampling method (**Deep DSM**, see Section 4.3) and the deep Gauss-Newton TV (**Deep GN-TV**, see Section 4.4). Further, we provide visual comparisons to the level set method, cf. Section 3.3, for which we do not present quantitative results. All learned reconstruction methods were trained on the training dataset described in Section 5.2. For the model-based approaches, we tuned hyperparameters, e.g., the regularization parameter, on the validation set.

Table 1: Performance comparison of model-based and learned methods for the full set of current patterns on the test set of the simulated ellipses. We also compare against a naive method which only outputs a constant conductivity equal to the background. We state the mean and standard deviation for all scores, except for the measurement error, where we provide the median and the 25% and 75% percentiles.

Method	Rel. $L^1$ -Error ( $\downarrow$ )	Rel. $L^2$ -Error ( $\downarrow$ )	DS ( $\uparrow$ )	DR ( $\approx 1$ )	Meas. Error ( $\downarrow$ )
<b>Lin-Rec</b>	$0.209 \pm 0.09$	$0.096 \pm 0.07$	$0.624 \pm 0.12$	$0.970 \pm 0.42$	$0.038 (0.001, 0.328)$
<b>D-bar</b>	$0.320 \pm 0.10$	$0.145 \pm 0.10$	$0.514 \pm 0.18$	$1.130 \pm 0.39$	$0.116 (0.087, 0.182)$
<b>L1-Sparsity</b>	$0.109 \pm 0.05$	$0.057 \pm 0.03$	$0.788 \pm 0.12$	$0.912 \pm 0.29$	$7.91e-4 (5.48e-4, 1.18e-3)$
<b>GN-TV</b>	$0.096 \pm 0.03$	$0.024 \pm 0.01$	$0.876 \pm 0.08$	$1.110 \pm 0.19$	$1.98e-5 (1.75e-5, 2.54e-5)$
<b>FC-UNet</b>	$0.035 \pm 0.02$	$0.011 \pm 0.01$	$0.958 \pm 0.02$	$1.041 \pm 0.09$	$3.25e-4 (2.40e-4, 5.14e-4)$
<b>Post-UNet</b>	$0.036 \pm 0.02$	$0.013 \pm 0.01$	$0.956 \pm 0.02$	$0.994 \pm 0.07$	$2.99e-4 (2.15e-4, 6.56e-4)$
<b>Deep D-bar</b>	$0.129 \pm 0.06$	$0.065 \pm 0.04$	$0.742 \pm 0.12$	$1.179 \pm 0.34$	$4.72e-3 (2.82e-3, 8.16e-3)$
<b>Deep DSM</b>	$0.084 \pm 0.03$	$0.035 \pm 0.02$	$0.882 \pm 0.06$	$1.058 \pm 0.18$	$7.36e-4 (4.21e-4, 2.19e-3)$
<b>Deep GN-TV</b>	$0.042 \pm 0.02$	$0.016 \pm 0.01$	$0.945 \pm 0.02$	$1.059 \pm 0.13$	$3.55e-4 (2.40e-4, 6.61e-4)$
Const. Background	$0.171 \pm 0.09$	$0.140 \pm 0.09$	$0.399 \pm 0.08$	$0.0 \pm 0.0$	$0.022 (0.008, 0.494)$

## 6.1 Simulated dataset

We evaluate all methods on the held-out test set of simulated ellipses. The test set shares the same characteristics, e.g., the number of inclusions, noise levels, and intensity values, as the training and validation sets, which makes it an in-distribution benchmark. Quantitative results are presented in Table 1, including the mean and standard deviation of the evaluation scores. We observe that the measurement error is not symmetric, therefore we provide the median value and the 25% and 75% percentiles. Table 1 also includes the performance scores for a constant background reconstruction, which serves solely as a baseline for comparison. Exemplary reconstructions are shown in Figure 2.

The linearized reconstruction method and D-bar produce overly smooth reconstructions and it is difficult to distinguish inclusions, as illustrated in the first row of Figure 2. The variational methods, L1-Sparsity and GN-TV, show significant improvement over these direct reconstruction techniques, although these iterative methods come with a higher computational cost. Specifically, GN-TV generates sharper conductivity distributions, though it still suffers from the typical staircasing artifacts [Bredies et al., 2010], one well known drawback of the total variation penalty. All model-based methods struggle to distinguish between closely located inclusions with similar intensity values, due to the severely ill-posed nature of the EIT inverse problem. However, in the visual results, the level set method is mostly able to provide a good location of the inclusions. However, for some reconstructions, e.g., the first row in Figure 2, small artifacts are clearly visible.

In contrast, learned reconstruction methods effectively leverage the characteristics of the training set and better identify inclusions, resulting in superior performance metrics, cf. Table 1. Both post-processing methods (Post-UNet, which takes Lin-Rec as input, and the Deep D-bar method, which uses D-bar reconstructions as input) demonstrate impressive improved performance over their model-based counterparts. In particular, the Post-UNet is able to improve the relative  $L^1$ -error to 0.036, compared to 0.209 for Lin-Rec. Similarly, Deep D-bar achieves a relative  $L^1$ -error of 0.129 compared to 0.320 for the original D-bar method. These post-processing methods are able to transform the smooth initial reconstructions into sharper outputs. (Generally better initial reconstructions lead to more accurate postprocessing results.) However, the performance is also limited by the accuracy of the initial reconstruction. The Deep DSM provides better reconstructions than Deep D-bar but falls short of the performance achieved by Deep GN-TV or FC-UNet. Additionally, while the Deep DSM reconstructions are relatively sharp, they occasionally exhibit slight distortions and fail to localize inclusions precisely (see the second row in Figure 2). The comparison between GN-TV and its learned counterpart Deep GN-TV indicates that the learned method is also able to improve the performance of the classical Gauss-Newton method.

The best-performing method, based on relative  $L^1$  and  $L^2$  errors as well as the Dice Score, is the FC-UNet on the in-distribution test set. This fully-trained method excels at recovering the locations and shapes of inclusions for phantoms with similar characteristics as the training data. However, on the out-of-distribution dataset, the performance of the FC-UNet drops significantly, see Table 2. This is attributed to the fact that the FC-UNet does not integrate any physical information of the underlying EIT inverse problem and is entirely data-dependent. In Figure 3, one can see that the FC-UNet reconstructs two ellipses in the shape of the "L" instead of an actual "L", clearly indicating the hallucination effect on the out-of-distribution test data. Also, for this task, the level set method provides an accurate localisation, but underestimates the volume, possibly due to an imprecise choice of the penalty parameter  $\alpha$ .

Table 2: Performance comparison of model-based and learned methods for the full set of current patterns on the simulated out-of-distribution set. We also compare against a naive method which only outputs a constant conductivity equal to the background. We state the mean and standard deviation for all scores, except for the measurement error, where we provide the median and the 25% and 75% percentiles.

Method	Rel. $L^1$ -Error ( $\downarrow$ )	Rel. $L^2$ -Error ( $\downarrow$ )	DS ( $\uparrow$ )	DR ( $\approx 1$ )	Meas. Error ( $\downarrow$ )
<b>Lin-Rec</b>	$0.168 \pm 0.02$	$0.076 \pm 0.01$	$0.581 \pm 0.07$	$0.586 \pm 0.23$	$5.56e-4$ ( $3.67e-4, 3.24e-3$ )
<b>D-bar</b>	$0.272 \pm 0.01$	$0.111 \pm 0.01$	$0.589 \pm 0.16$	$1.242 \pm 0.32$	$8.98e-2$ ( $8.95e-2, 9.92e-2$ )
<b>L1-Sparsity</b>	$0.114 \pm 0.05$	$0.078 \pm 0.03$	$0.721 \pm 0.17$	$0.532 \pm 0.27$	$8.08e-4$ ( $5.57e-4, 9.70e-4$ )
<b>GN-TV</b>	$0.104 \pm 0.02$	$0.037 \pm 0.01$	$0.835 \pm 0.03$	$0.893 \pm 0.15$	$1.70e-5$ ( $1.67e-5, 1.87e-5$ )
<b>FC-UNet</b>	$0.071 \pm 0.02$	$0.034 \pm 0.01$	$0.880 \pm 0.03$	$0.825 \pm 0.10$	$2.36e-4$ ( $2.22e-4, 2.86e-4$ )
<b>Post-UNet</b>	$0.065 \pm 0.02$	$0.031 \pm 0.01$	$0.891 \pm 0.03$	$0.840 \pm 0.08$	$2.09e-4$ ( $1.96e-4, 2.28e-4$ )
<b>Deep D-bar</b>	$0.100 \pm 0.02$	$0.057 \pm 0.01$	$0.711 \pm 0.14$	$1.050 \pm 0.30$	$7.71e-4$ ( $6.18e-4, 1.25e-3$ )
<b>Deep DSM</b>	$0.078 \pm 0.02$	$0.038 \pm 0.01$	$0.869 \pm 0.03$	$0.876 \pm 0.12$	$1.66e-4$ ( $1.57e-4, 1.68e-4$ )
<b>Deep GN-TV</b>	$0.064 \pm 0.02$	$0.033 \pm 0.01$	$0.882 \pm 0.03$	$0.901 \pm 0.10$	$2.08e-4$ ( $1.86e-4, 2.45e-4$ )

On this generalisation task the best methods are Deep GN-TV (for relative  $L^1$  error) and the Post-UNet (for relative  $L^2$  error and the dice score), which directly incorporate the classical algorithms, either as part of the architecture or as the input. These observations indicate the importance of accurately incorporating the information of the physical model into the learned algorithms, in order to improve their robustness.

## 6.2 KIT4 dataset

We present quantitative results for the KIT4 dataset in Table 3. The KIT4 dataset is divided into subsets as follows: 'Set 1–Set 5', which include at most three different inclusions in the watertank; 'Set 6', which features a foam layer on the boundary; 'Set 7', containing a pumpkin; and 'Set 8', which has a foam layer near the boundary. The first subset 'Set 1–Set 5' is the most similar to the original training data, albeit with different shapes of inclusions. The other subsets exhibit significantly different characteristics. All models were applied directly to the KIT4 data without re-training or fine-tuning hyperparameters. However, we remind that the Dice score used here may not be the ideal measure to reflect image quality and should be interpreted as a secondary indicator of reconstruction quality. Visual inspection the qualitative reconstructions remains important for the KIT4 data.

For the simulated data, the FC-UNet achieves the highest performance. However, this trend does not hold for the KIT4 data. On 'Set 1–Set 5', the best-performing method is the Deep GN-TV. This is likely because Deep GN-TV incorporates classical Gauss-Newton steps, which generalize better to new data. Visual results for this scenario are presented in Figures 4 and 5. These figures show that classical methods, e.g., L1-Sparsity or GN-TV, can largely recover the inclusions but introduce a number of image artifacts. Further, for 'Set 1–Set 5' the level set method is able to produce accurate segmentations. In particular, for the second row in Figure 4, the level set method is the only method which is able to recover the shape of the triangle, showing its potential for EIT.

For the remaining KIT4 subsets, all methods fail to yield satisfactory results. The presence of an additional foam layer, either on or near the boundary, drastically alters the measurement setup, and none of the methods can effectively adapt to these changes. For example, L1-Sparsity uses an  $H_0^1(\Omega)$  gradient (i.e., zero-boundary conditions, and thus the conductivity distributions with inclusions on the boundary as in 'Set 8' cannot be modelled adequately, since the algorithm cannot change from the initial background conductivity.

## 7 Conclusion

In this paper, we have presented a numerical comparison of several widely used model-based and learned methods for image reconstruction in EIT. The study evaluates their performance across multiple criteria using three distinct datasets (both simulated and measured data), highlighting the diverse strengths of each method. The key characteristics of each approach are summarized below. It is important to note that the choice of an optimal algorithm depends heavily on the specific experimental context and the intended application of the EIT reconstruction, whether for diagnosis or further processing.

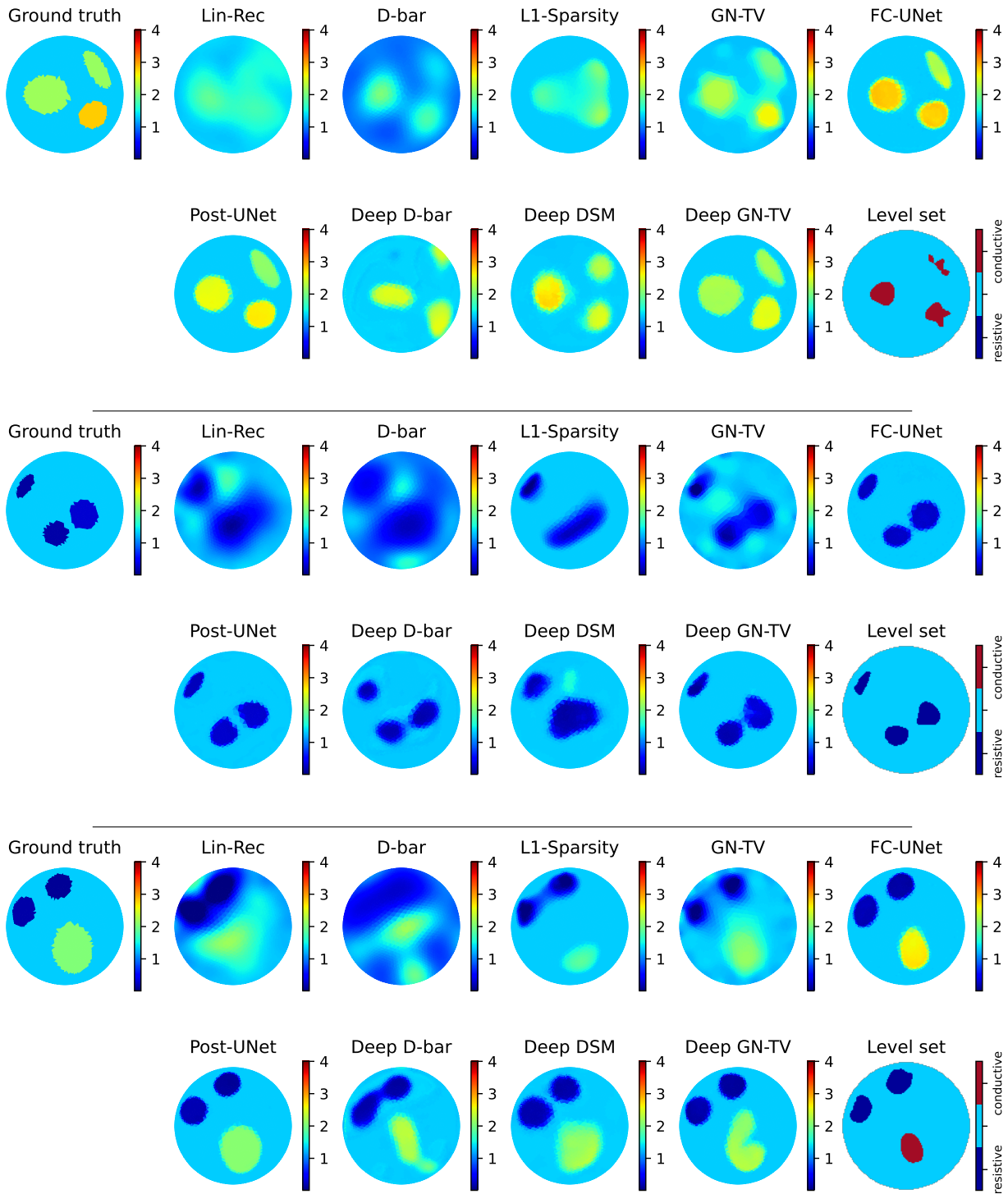


Figure 2: Reconstructions for the different methods on the test set of simulated ellipses. The level set method produce segmentations, with blue regions representing resistive inclusions and red regions representing conductive inclusions.

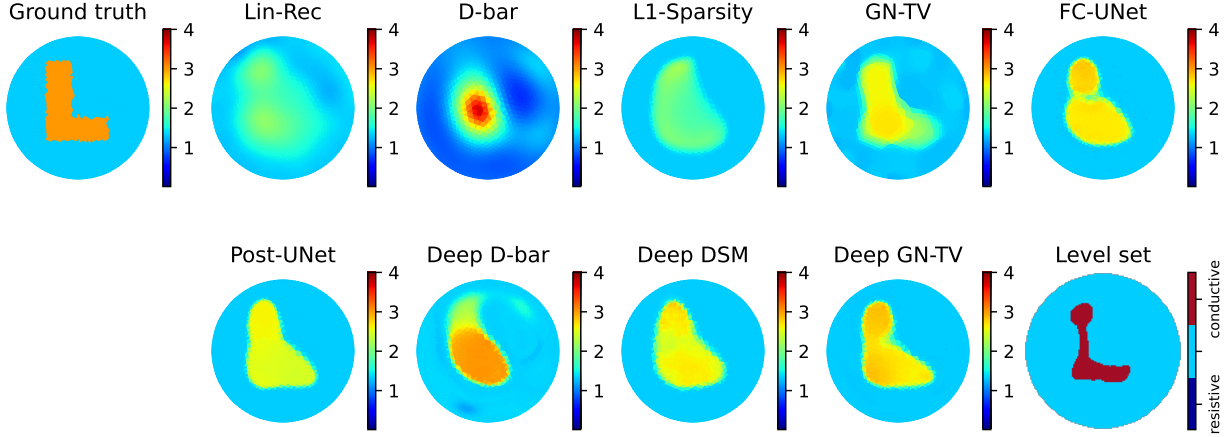


Figure 3: Reconstruction for out-of-distribution phantom. We can see that most of the learned methods stay close to the training distribution of ellipses. In particular the FC-UNet reconstructs two ellipses instead of the "L".

Table 3: Performance comparison of model-based and learned methods for the full set of current patterns on the KIT4 dataset. For KIT4 no ground truth data is available. We compute the Dice Score using a hand-annotated segmentation mask. Set 1 - Set 5 contains inclusions inside the water-tank. Set 6 has an additional foam layer on the boundary. Set 7 contains a slice of pumpkin. Finally, Set 8 contains additional foam near the boundary. We give the dice score (DS) and the measurement error (Meas. Error).

Method	Set 1 - Set 5			Set 6		Set 7		Set 8	
	DS ( $\uparrow$ )	Meas. Error ( $\downarrow$ )	DS ( $\uparrow$ )	Meas. Error ( $\downarrow$ )	DS ( $\uparrow$ )	Meas. Error ( $\downarrow$ )	DS ( $\uparrow$ )	Meas. Error ( $\downarrow$ )	DS ( $\uparrow$ )
<b>Lin-Rec</b>	0.533	0.038	0.357	91.99	0.313	0.010	0.395	0.173	
<b>D-bar</b>	0.465	0.167	0.251	0.136	0.407	0.472	0.425	0.405	
<b>L1-Sparsity</b>	0.661	0.0015	0.603	0.0031	0.241	0.005	0.629	0.045	
<b>GN-TV</b>	0.697	0.00037	0.114	0.0004	0.428	0.0002	0.228	0.00189	
<b>FC-UNet</b>	0.761	0.0014	0.378	0.0718	0.345	0.0379	0.486	0.496	
<b>Post-UNet</b>	0.694	0.001	0.381	0.0459	0.309	0.0344	0.575	0.0343	
<b>Deep D-bar</b>	0.695	0.0049	0.408	0.0602	0.493	0.0885	0.537	0.4424	
<b>Deep DSM</b>	0.770	0.0069	0.350	0.0419	0.255	0.0149	0.615	0.230	
<b>Deep GN-TV</b>	0.775	0.0013	0.408	0.063	0.276	0.0124	0.539	0.197	

## 7.1 Discussion of results on the different data sets

Although the methods and datasets vary widely, certain general observations can be made. Let us first comment on the model-based reconstruction methods and how they perform on the standardized set of simulated ellipsoidal data. Arguably, Lin-Rec is the most commonly used model-based method for EIT and it constitutes somewhat the baseline algorithm for this application. For the given noise level of 0.5% the  $L^p$ -error estimates are in the range of 10 – 20% and the measurement error is approximately 4%, which is in the expected range for such a severely ill-posed problem and given the limited data for reconstruction. The D-bar method does not reach these values, which is primarily caused by the cut-off radius in the scattering data which leads to a strong blurring. (Nevertheless, in theory, it is a proven regularization strategy [Knudsen et al., 2009]). More advanced model-based reconstruction methods such as L1-Sparsity and GN-TV perform significantly better. Not surprisingly, if GN-TV is combined with unrolling techniques, the numerical results get even better. Exploiting the training data cuts the  $L^p$ -errors in half for Deep GN-TV. Notably, FC-UNet and Post-UNet perform even better. Both are on equal levels overall and are the winners in terms of  $L^p$ -accuracy for the simulated in-distribution data. Their error levels are between 1.5 – 2% for  $L^2$ -errors and measurement errors are below 0.1%.

In general, all five learned reconstruction methods based on either post-processing or unrolling surpass the model-based methods for in-distribution simulated data. However, the picture changes for out-of-distribution experiments, which test their potential for generalization. The error levels for the model-based approaches stay roughly the same, while the learned concepts show a significant increase in the error levels. This agrees well with the intuition: the learned reconstructors were only trained on ellipsoidal data and now try to approximate the out-of-distribution examples as

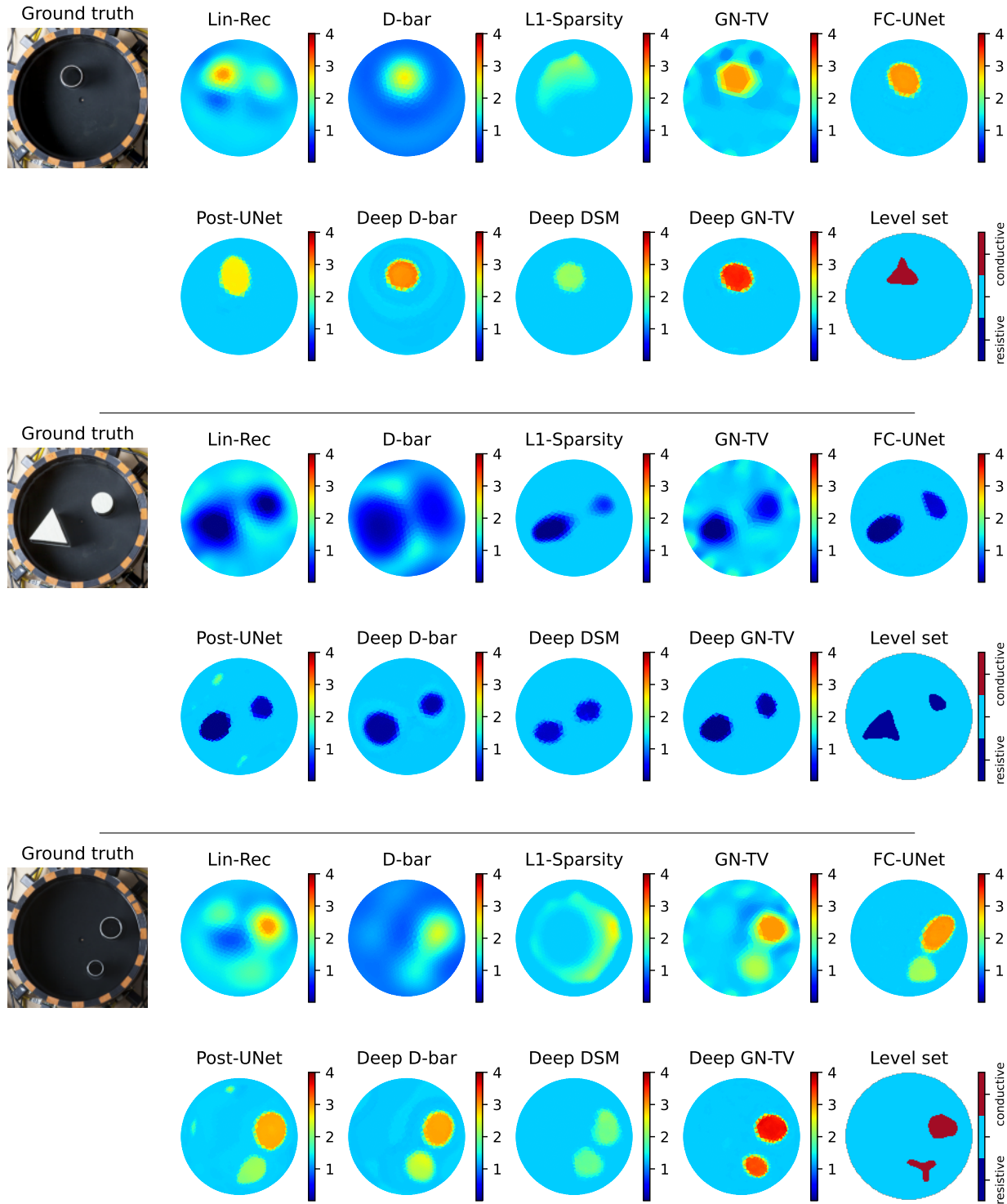


Figure 4: Reconstructions for KIT4 measurements. Top to bottom: Set 1.3, Set 2.1, Set 2.5. The level set method produce segmentations, with blue regions representing resistive inclusions and red regions representing conductive inclusions.

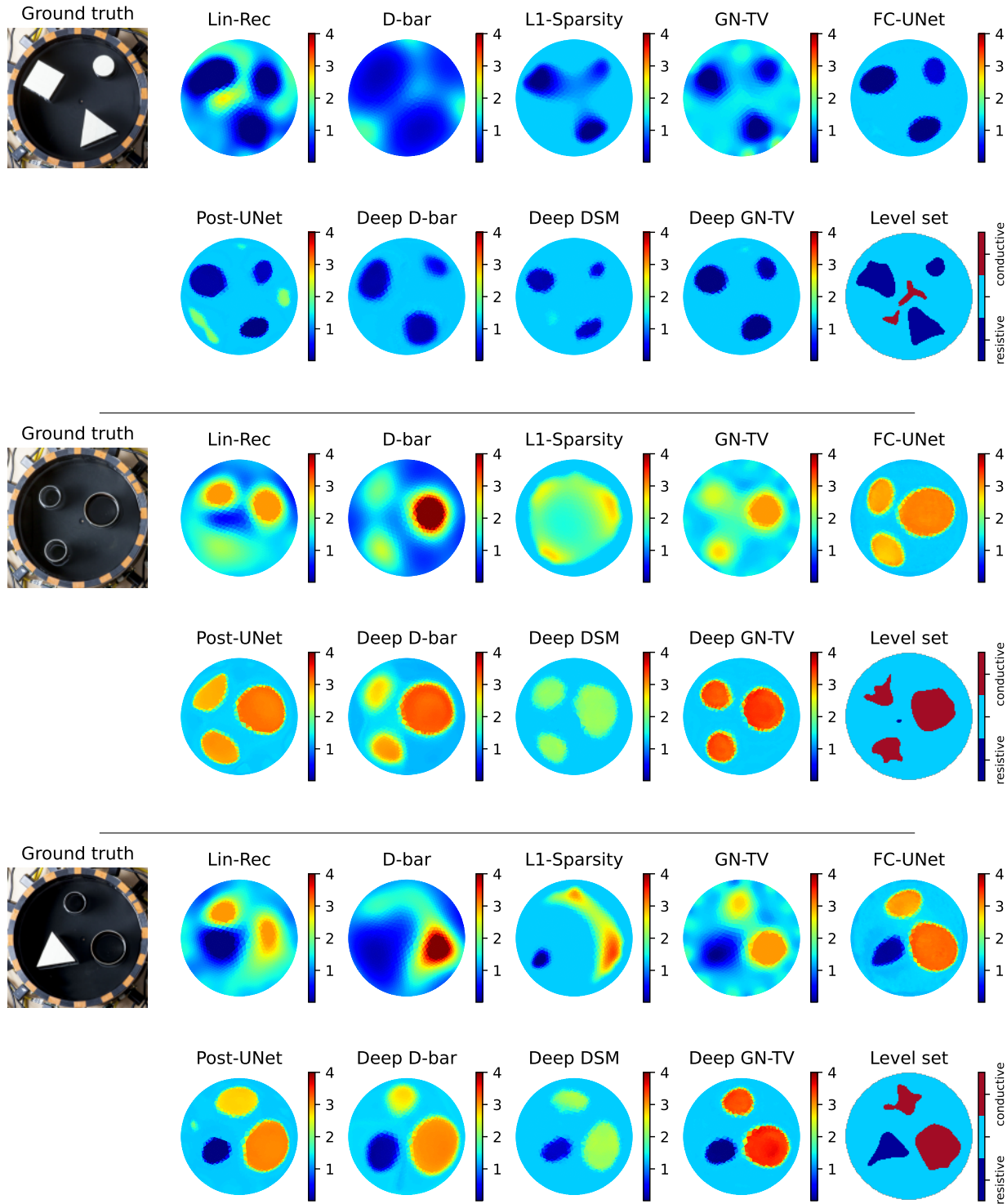


Figure 5: Reconstructions for KIT4 measurements. Top to bottom: Set 3.1, Set 3.4, Set 5.2. The level set method produce segmentations, with blue regions representing resistive inclusions and red regions representing conductive inclusions.

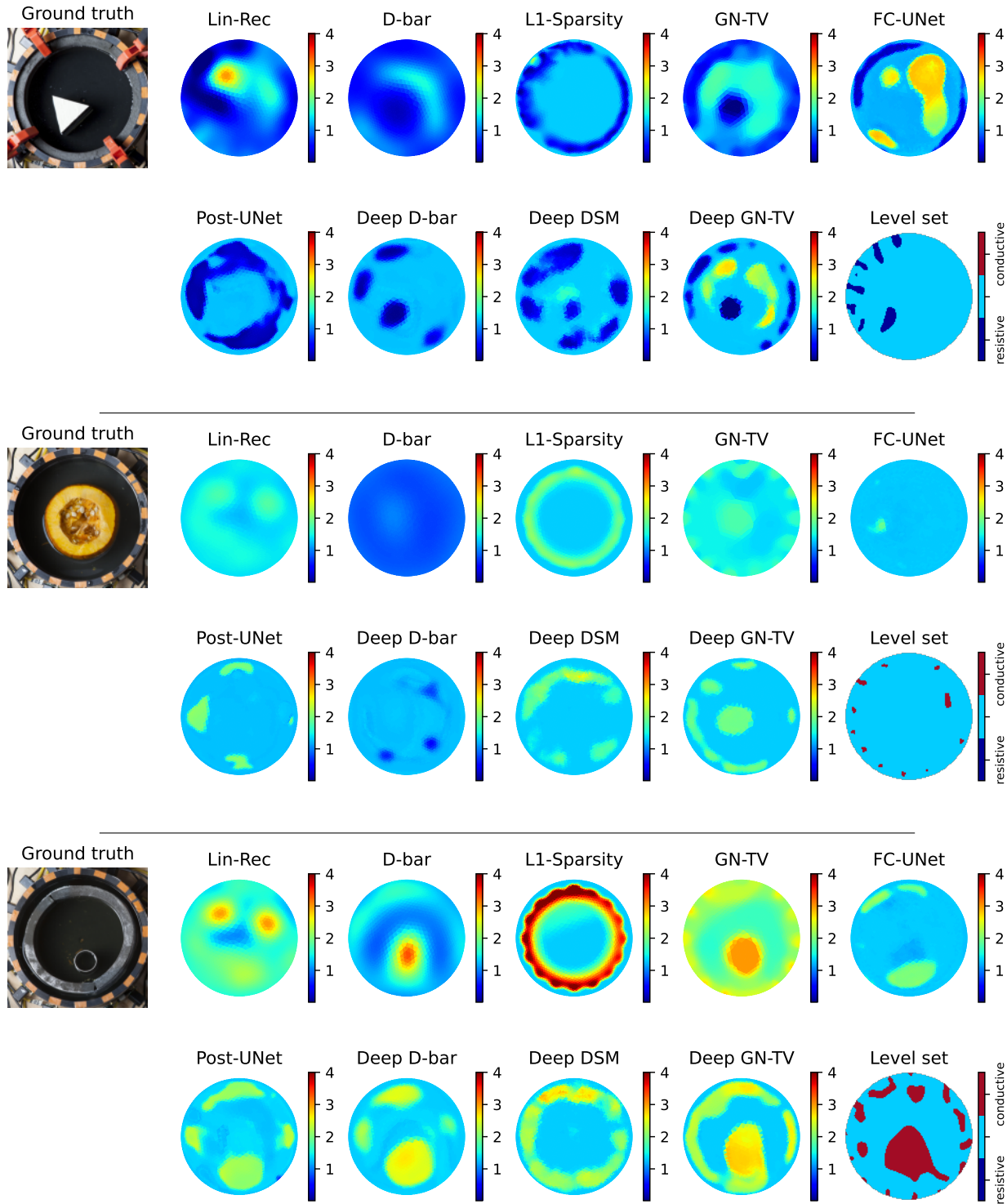


Figure 6: Reconstructions for KIT4 measurements. Top to bottom: Set 6.2, Set 7.1, Set 8.2. The level set method produce segmentations, with blue regions representing resistive inclusions and red regions representing conductive inclusions.

superpositions of ellipsoids. Still, the learned methods do slightly outperform the model-based methods. The best methods, both in terms of quantitative numerical error values and also by visual inspection, are Post-UNet and Deep GN-TV. However, we should stress that the model-based GN-TV and partially L1-Sparsity produce results in the same range of errors, despite the differences in terms of visual inspection.

When considering the generalizability of these learned methods, it is important to take into account the number of trainable parameters. The FC-UNet has approximately 11 million parameters, while Post-UNet and Deep D-bar have about 6 million parameters each. Deep GN-TV greatly reduces the parameter count to 0.7 million. The reduced parameter count of Deep GN-TV, combined with the integration of model-based GN-TV step, likely contributes to its relatively better generalization on out-of-distribution data, as it may mitigate overfitting to the training distribution.

Both L1-Sparsity and GN-TV are very stable when they are applied to out-of-distribution data, with only a minor drop in all quality measures. This is definitely a significant advantage of model-based methods, and indeed they do not rely on previously seen similar cases and still perform very well. Meanwhile, the level set method aims at identifying the locations and shapes of the objects rather than at reconstructing the conductivity values. The results show its general potential for EIT, and the results for the out-of-distribution example are amazing.

Finally, let us comment on the performance on the real data set KIT4. Visual inspection of the results demonstrates the complexity of the problem. The obtained reconstructions widely vary in quality and all are open for further improvement. Specifically, the results between the simplistic targets in Figures 4 and 5 compared to the structured targets in Figure 6 are drastically different. In the former case, all learned reconstruction methods performed well and generalize from the simulated training to the in-distribution test set, for the Post-UNet some residual artifacts seem to be caused by the linearized reconstructions, while Deep D-bar and Deep DSM performed best out of the post-processing type approaches. Notably, L1-Sparsity and Post-UNet, which did very well on simulated data, fails to resolve the inner structures of the KIT4 data set, especially for the structured targets in Figure 6. Similarly, the adaptation of the level set method to real data needs further refinement.

Visual inspection shows GN-TV and Deep GN-TV as clear winners: they are the only methods that allow a direct visual identification of the inner major structures. Surprisingly, this is much less mirrored by the numerical error values. Still GN-TV and Deep GN-TV give the best values, but L1-Sparsity performs very well when using dice score as error measure. This might be due to the structure of the phantoms, L1-Sparsity perfectly reconstructs the outer edges, which dominate in Dice score the inner structures. Nonetheless, in practice the full evaluation has also to be considered in view of the underlying task which usually involves further processing or classification tasks on the reconstructions.

## 7.2 Summary

Fully-learned methods, e.g. the FC-UNet, demonstrate remarkable performance on the in-distribution test set. However, one big limitation of these methods is the strong dependence on the specific measurement settings they were trained on, and thus limited portability to different scenarios. Any change in the measurement process, e.g., varying the injection patterns and the number of electrodes, necessitates re-training the model from the scratch, which can be computationally expensive and requires a new training dataset. In contrast, hybrid approaches, e.g., Post-UNet or Deep GN-TV, offer greater adaptability. These methods can be used for different measurement settings without requiring extensive retraining, albeit sometimes at the cost of reduced reconstruction performance. This adaptability comes from the integration of the physical model (i.e., the FEM model) into the architecture, which indirectly encodes the flexibility with respect to the measurement configuration.

The ultimate goal should be to develop flexible learned reconstruction methods that can operate independently of both the measurement settings (e.g., varying injection patterns), geometry of the domain (e.g., irregular or non-circular domains) and boundary conditions (e.g., different number and size of electrodes). Achieving this level of generalization requires addressing several outstanding challenges, including designing domain independent network architectures. One option would be to make use of advances both in neural operators [Azizzadenesheli et al., 2024] and graph neural networks to build discretization invariant architectures.

Our experimental results highlight one notable limitation of learned methods for image reconstruction: models trained exclusively on simulated data may fail to generalize effectively to real-world measurements with new characteristics. This discrepancy show the need for methods adapting pre-trained models to new, unseen data distributions. One promising avenue to address this issue involves post-training or fine-tuning strategies, such as test-time training (TTT) [Darestani et al., 2022, Barbano et al., 2022]. These approaches allow a model to adapt dynamically, after initial training, to the distribution of the test data. For instance, leveraging an unsupervised loss function during TTT can enable fine-tuning based solely on the measured data, potentially bridging the gap between simulated and real-world data. Recent work has also shown that training DNNs in a purely unsupervised manner can be effective for EIT image reconstruction [Liu et al., 2023], highlighting the potential of incorporating these unsupervised training strategies as

a fine-tuning step. Future research should explore generalization capabilities, with a focus on integrating fine-tuning methods into existing learned reconstruction methods.

## Acknowledgments

Alexander Denker acknowledges support by the UK EPSRC programme grant EP/V026259/1. Bangti Jin is supported by Hong Kong RGC General Research Fund (Project 14306423 and Project 14306824), and a start-up fund from The Chinese University of Hong Kong. Andreas Hauptmann is supported by the Research Council of Finland with the Flagship of Advanced Mathematics for Sensing Imaging and Modelling Project No. 359186, Centre of Excellence of Inverse Modelling and Imaging Project No. 353093, and the Academy Research Fellow Project No. 338408. Kim Knudsen is supported by the Villum Foundation (grant no. 25893) and acknowledges computational assistance from Chao Zhang. Derick Nganyu Tanyu acknowledges support by the Deutsche Forschungsgemeinschaft (DFG, German Research Foundation) - project number 281474342/GRK2224/1 "Pi3 : Parameter Identification - Analysis, Algorithms, Applications". Peter Maass acknowledges support by the Sino-German Center for Research Promotion (CDZ) within the Sino-German Mobility Programme "Inverse problems – theories, methods and implementations" (Grant No. M-0187). Fabio Margotti acknowledges the support of the Brazilian funding agency National Council for Scientific and Technological Development (CNPq - Grant 406206/2021-0).

## References

- B. J. Adesokan, B. Jensen, B. Jin, and K. Knudsen. Acousto-electric tomography with total variation regularization. *Inverse Problems*, 35(3):035008, 25, 2019. ISSN 0266-5611,1361-6420. doi: 10.1088/1361-6420/aaece5. URL <https://doi.org/10.1088/1361-6420/aaece5>.
- A. Adler and R. Guardo. A neural network image reconstruction technique for electrical impedance tomography. *IEEE Trans. Med. Imag.*, 13(4):594–600, 1994.
- J. Adler and O. Öktem. Solving ill-posed inverse problems using iterative deep neural networks. *Inverse Problems*, 33(12):124007, 2017.
- J. Adler and O. Öktem. Learned primal-dual reconstruction. *IEEE Trans. Med. Imag.*, 37(6):1322–1332, 2018.
- G. S. Alberti, J. Hertrich, M. Santacesaria, and S. Sciuotto. Manifold learning by mixture models of vae's for inverse problems. *J. Mach. Learn. Res.*, 25:1–35, 2024.
- G. S. Alberti, D. Lazzaro, S. Morigi, L. Ratti, and M. Santacesaria. Deep unfolding network for nonlinear multi-frequency electrical impedance tomography. Preprint, arXiv:2507.16678, 2025.
- G. Alessandrini. Stable determination of conductivity by boundary measurements. *Appl. Anal.*, 27(1-3):153–172, 1988.
- A. M. A. Alghamdi, M. S. Carøe, J. M. Everink, J. S. Jørgensen, K. Knudsen, J. T. K. Nielsen, A. K. Rasmussen, R. K. H. Sørensen, and C. Zhang. Spatial regularization and level-set methods for experimental electrical impedance tomography with partial data. *Appl. Math. Mod. Chall.*, 2(2):165–186, 2024. doi: 10.3934/ammc.2024013. URL <https://www.aims.science/article/id/667001855a42b314c5bfc724>.
- V. Antun, F. Renna, C. Poon, and A. C. Hansen. On instabilities of deep learning in image reconstruction and the potential costs of AI. *Proc. Nat. Acad. Sci.*, 117(48):30088–30095, 2020. doi: 10.1073/pnas.1907377117.
- S. Arridge, P. Maass, O. Öktem, and C.-B. Schönlieb. Solving inverse problems using data-driven models. *Acta Numer.*, 28:1–174, 2019.
- K. Astala and L. Päivärinta. Calderón's inverse conductivity problem in the plane. *Ann. of Math.* (2), 163(1):265–299, 2006. ISSN 0003-486X,1939-8980. doi: 10.4007/annals.2006.163.265. URL <https://doi.org/10.4007/annals.2006.163.265>.
- K. Azizzadenesheli, N. Kovachki, Z. Li, M. Liu-Schiaffini, J. Kossaifi, and A. Anandkumar. Neural operators for accelerating scientific simulations and design. *Nature Rev. Phys.*, 6(5):320–328, 2024.
- L. Bar and N. Sochen. Strong solutions for pde-based tomography by unsupervised learning. *SIAM J. Imag. Sci.*, 14(1):128–155, 2021.
- R. Barbano, J. Leuschner, M. Schmidt, A. Denker, A. Hauptmann, P. Maass, and B. Jin. An educated warm start for deep image prior-based micro ct reconstruction. *IEEE Trans. Comput. Imag.*, 8:1210–1222, 2022.
- J. Barzilai and J. M. Borwein. Two-point step size gradient methods. *IMA J. Numer. Anal.*, 8(1):141–148, 1988. ISSN 0272-4979. doi: 10.1093/imanum/8.1.141. URL <https://doi.org/10.1093/imanum/8.1.141>.

- J. Bikowski and J. L. Mueller. 2D EIT reconstructions using Calderón's method. *Inverse Probl. Imaging*, 2(1):43–61, 2008. ISSN 1930-8337,1930-8345. doi: 10.3934/ipi.2008.2.43. URL <https://doi.org/10.3934/ipi.2008.2.43>.
- T. Bonesky, K. Bredies, D. A. Lorenz, and P. Maass. A generalized conditional gradient method for nonlinear operator equations with sparsity constraints. *Inverse Problems*, 23(5):2041–2058, 2007. ISSN 0266-5611,1361-6420. doi: 10.1088/0266-5611/23/5/014. URL <https://doi.org/10.1088/0266-5611/23/5/014>.
- L. Borcea. Electrical impedance tomography. *Inverse Problems*, 18(6):R99–R136, 2002. ISSN 0266-5611,1361-6420. doi: 10.1088/0266-5611/18/6/201. URL <https://doi.org/10.1088/0266-5611/18/6/201>.
- A. Borsic, B. M. Graham, A. Adler, and W. R. Lionheart. In vivo impedance imaging with total variation regularization. *IEEE Trans. Med. Imag.*, 29(1):44–54, 2009.
- K. Bredies, D. A. Lorenz, and P. Maass. A generalized conditional gradient method and its connection to an iterative shrinkage method. *Comput. Optim. Appl.*, 42(2):173–193, 2009. ISSN 0926-6003,1573-2894. doi: 10.1007/s10589-007-9083-3. URL <https://doi.org/10.1007/s10589-007-9083-3>.
- K. Bredies, K. Kunisch, and T. Pock. Total generalized variation. *SIAM J. Imaging Sci.*, 3(3):492–526, 2010. ISSN 1936-4954. doi: 10.1137/090769521. URL <https://doi.org/10.1137/090769521>.
- S. C. Brenner and L. R. Scott. *The Mathematical Theory of Finite Element Methods*, volume 15 of *Texts in Applied Mathematics*. Springer, New York, third edition, 2008. ISBN 978-0-387-75933-3. doi: 10.1007/978-0-387-75934-0. URL <https://doi.org/10.1007/978-0-387-75934-0>.
- A.-P. Calderón. On an inverse boundary value problem. In *Seminar on Numerical Analysis and its Applications to Continuum Physics (Rio de Janeiro, 1980)*, pages 65–73. Soc. Brasil. Mat., Rio de Janeiro, 1980.
- X. Cao, Q. Ding, and Z. Xiaoqun. Multi-scale frequency-enhanced deep D-bar method for electrical impedance tomography. *Inverse Problems*, 41(8):085005, 2025. doi: 10.1088/1361-6420/adf255.
- S. Cen, B. Jin, K. Shin, and Z. Zhou. Electrical impedance tomography with deep Calderon method. *J. Comput. Phys.*, 493:112427, 2023.
- J. E. Chambers, P. B. Wilkinson, A. L. Weller, P. I. Meldrum, R. D. Ogilvy, and S. Caunt. Mineshaft imaging using surface and crosshole 3D electrical resistivity tomography: a case history from the East Pennine Coalfield, UK. *J. Appl. Geophys.*, 62(4):324–337, 2007.
- T. F. Chan and X.-C. Tai. Level set and total variation regularization for elliptic inverse problems with discontinuous coefficients. *J. Comput. Phys.*, 193(1):40–66, 2004. ISSN 0021-9991,1090-2716. doi: 10.1016/j.jcp.2003.08.003. URL <https://doi.org/10.1016/j.jcp.2003.08.003>.
- J. Chen and H. Liu. Implicit neural shape optimization for 3D high-contrast electrical impedance tomography. Preprint, arXiv:2505.16487, 2025.
- Z. Chen, Y. Yang, J. Jia, and P. Bagnaninchi. Deep learning based cell imaging with electrical impedance tomography. In *2020 IEEE International Instrumentation and Measurement Technology Conference (I2MTC)*, pages 1–6, 2020. doi: 10.1109/I2MTC43012.2020.9128764.
- Z. Chen, J. Xiang, P.-O. Bagnaninchi, and Y. Yang. MMV-Net: A multiple measurement vector network for multifrequency electrical impedance tomography. *IEEE Trans. Neural Networks Learn. System*, 34(11):8938–8949, 2023. doi: 10.1109/TNNLS.2022.3154108.
- M. Cheney. The linear sampling method and the MUSIC algorithm. *Inverse Problems*, 17(4):591–595, 2001. ISSN 0266-5611,1361-6420. doi: 10.1088/0266-5611/17/4/301. URL <https://doi.org/10.1088/0266-5611/17/4/301>.
- M. Cheney and D. Isaacson. Distinguishability in impedance imaging. *IEEE Trans. Biomed. Imag.*, 39(8):852–860, 1992. doi: 10.1109/10.148393.
- M. Cheney, D. Isaacson, J. C. Newell, S. Simske, and J. Goble. NOSER: An algorithm for solving the inverse conductivity problem. *Int. J. Imag. Syst. Tech.*, 2:66–75, 1990.
- Y. T. Chow, K. Ito, and J. Zou. A direct sampling method for electrical impedance tomography. *Inverse Problems*, 30(9):095003, 2014.
- E. T. Chung, T. F. Chan, and X.-C. Tai. Electrical impedance tomography using level set representation and total variational regularization. *J. Comput. Phys.*, 205(1):357–372, 2005. ISSN 0021-9991,1090-2716. doi: 10.1016/j.jcp.2004.11.022. URL <https://doi.org/10.1016/j.jcp.2004.11.022>.
- F. Colibazzi, D. Lazzaro, S. Morigi, and A. Samoré. Deep-plug-and-play proximal Gauss-Newton method with applications to nonlinear, ill-posed inverse problems. *Inverse Probl. Imaging*, 17(6):1226–1248, 2023. ISSN 1930-8337,1930-8345. doi: 10.3934/ipi.2023014. URL <https://doi.org/10.3934/ipi.2023014>.

- Y.-H. Dai, W. W. Hager, K. Schittkowski, and H. Zhang. The cyclic Barzilai-Borwein method for unconstrained optimization. *IMA J. Numer. Anal.*, 26(3):604–627, 2006. ISSN 0272-4979,1464-3642. doi: 10.1093/imanum/drl006. URL <https://doi.org/10.1093/imanum/drl006>.
- J. Dardé and S. Staboulis. Electrode modelling: the effect of contact impedance. *ESAIM Math. Model. Numer. Anal.*, 50(2):415–431, 2016. ISSN 2822-7840,2804-7214. doi: 10.1051/m2an/2015049. URL <https://doi.org/10.1051/m2an/2015049>.
- M. Z. Darestani, J. Liu, and R. Heckel. Test-time training can close the natural distribution shift performance gap in deep learning based compressed sensing. In *International Conference on Machine Learning*, pages 4754–4776. PMLR, 2022.
- I. Daubechies, M. Defrise, and C. De Mol. An iterative thresholding algorithm for linear inverse problems with a sparsity constraint. *Comm. Pure Appl. Math.*, 57(11):1413–1457, 2004. ISSN 0010-3640,1097-0312. doi: 10.1002/cpa.20042. URL <https://doi.org/10.1002/cpa.20042>.
- F. Delbary and K. Knudsen. Numerical nonlinear complex geometrical optics algorithm for the 3d calderón problem. *Inverse Probl. Imaging*, 8(4):991–1012, 2014. ISSN 19308345, 19308337. doi: 10.3934/ipi.2014.8.991.
- A. Denker, Z. Kereta, I. Singh, T. Freudenberg, T. Kluth, P. Maass, and S. Arridge. Data-driven approaches for electrical impedance tomography image segmentation from partial boundary data. *Appl. Math. Mod. Chall.*, 2(2):119–139, 2024. doi: 10.3934/ammc.2024005. URL <https://www.aims sciences.org/article/id/664c6606abc893368bc65c4d>.
- P. Dhariwal and A. Nichol. Diffusion models beat gans on image synthesis. In *Advances in Neural Information Processing Systems*, volume 34, pages 8780–8794, 2021.
- D. C. Dobson and F. Santosa. An image-enhancement technique for electrical impedance tomography. *Inverse Problems*, 10(2):317–334, 1994.
- M. Dodd and J. L. Mueller. A real-time D-bar algorithm for 2-D electrical impedance tomography data. *Inverse Probl. Imaging*, 8(4):1013–1031, 2014.
- R. Ellis and D. Oldenburg. Applied geophysical inversion. *Geophys. J. Int.*, 116(1):5–11, 1994.
- H. W. Engl, M. Hanke, and A. Neubauer. *Regularization of inverse problems*. Kluwer Academic Publishers Group, Dordrecht, 1996. ISBN 0-7923-4157-0.
- L. D. Faddeev. Increasing solutions of the Schrödinger equation. *Sov.-Phys. Dokl.*, 10:1033–5, 1966.
- Y. Fan and L. Ying. Solving electrical impedance tomography with deep learning. *J. Comput. Phys.*, 404:109119, 2020.
- A. Felisi and L. Rondi. Full discretization and regularization for the Calderón problem. *J. Differential Equations*, 410:513–577, 2024. ISSN 0022-0396,1090-2732. doi: 10.1016/j.jde.2024.07.040. URL <https://doi.org/10.1016/j.jde.2024.07.040>.
- M. Gehre, T. Kluth, A. Lipponen, B. Jin, A. Seppänen, J. P. Kaipio, and P. Maass. Sparsity reconstruction in electrical impedance tomography: an experimental evaluation. *J. Comput. Appl. Math.*, 236(8):2126–2136, 2012.
- M. Gehre, B. Jin, and X. Lu. An analysis of finite element approximation in electrical impedance tomography. *Inverse Problems*, 30(4):045013, 2014.
- P. Grisvard. *Elliptic Problems in Nonsmooth Domains*, volume 24 of *Monographs and Studies in Mathematics*. Pitman, Boston, MA, 1985. ISBN 0-273-08647-2.
- R. Guo and J. Jiang. Construct deep neural networks based on direct sampling methods for solving electrical impedance tomography. *SIAM J. Sci. Comput.*, 43(3):B678–B711, 2021.
- R. Guo, S. Cao, and L. Chen. Transformer meets boundary value inverse problems. In *The 11th International Conference of Learning Representation*, 2023. URL <https://openreview.net/forum?id=Hn1CZATopvr>.
- S. Hamilton, A. Hänninen, A. Hauptmann, and V. Kolehmainen. Beltrami-net: domain-independent deep d-bar learning for absolute imaging with electrical impedance tomography (a-eit). *Physiol. Meas.*, 40(7):074002, 2019.
- S. J. Hamilton and A. Hauptmann. Deep D-bar: Real-time electrical impedance tomography imaging with deep neural networks. *IEEE Trans. Med. Imag.*, 37(10):2367–2377, 2018.
- K. Hammernik, T. Klatzer, E. Kobler, M. P. Recht, D. K. Sodickson, T. Pock, and F. Knoll. Learning a variational network for reconstruction of accelerated mri data. *Magnetic Reson. Med.*, 79(6):3055–3071, 2018.
- M. Hanke. A regularizing Levenberg-Marquardt scheme, with applications to inverse groundwater filtration problems. *Inverse Problems*, 13(1):79–95, 1997. ISSN 0266-5611,1361-6420. doi: 10.1088/0266-5611/13/1/007. URL <https://doi.org/10.1088/0266-5611/13/1/007>.

- M. Hanke and M. Brühl. Recent progress in electrical impedance tomography. *Inverse Problems*, 19(6):S65–S90, 2003. ISSN 0266-5611,1361-6420. doi: 10.1088/0266-5611/19/6/055. URL <https://doi.org/10.1088/0266-5611/19/6/055>.
- B. Harrach. Uniqueness and lipschitz stability in electrical impedance tomography with finitely many electrodes. *Inverse problems*, 35(2):024005, 2019.
- B. Harrach and M. Ullrich. Monotonicity-based shape reconstruction in electrical impedance tomography. *SIAM J. Math. Anal.*, 45(6):3382–3403, 2013. ISSN 0036-1410,1095-7154. doi: 10.1137/120886984. URL <https://doi.org/10.1137/120886984>.
- A. Hauptmann. Approximation of full-boundary data from partial-boundary electrode measurements. *Inverse Problems*, 33(12):125017, 2017.
- A. Hauptmann, V. Kolehmainen, N. M. Mach, T. Savolainen, A. Seppänen, and S. Siltanen. Open 2d electrical impedance tomography data archive. *arXiv preprint arXiv:1704.01178*, 2017.
- A. Hauptmann, F. Lucka, M. Betcke, N. Huynh, J. Adler, B. Cox, P. Beard, S. Ourselin, and S. Arridge. Model-based learning for accelerated, limited-view 3-d photoacoustic tomography. *IEEE Trans. Med. Imag.*, 37(6):1382–1393, 2018.
- W. Herzberg, D. B. Rowe, A. Hauptmann, and S. J. Hamilton. Graph convolutional networks for model-based learning in nonlinear inverse problems. *IEEE Trans. Comput. Imag.*, 7:1341–1353, 2021. doi: 10.1109/TCI.2021.3132190.
- W. Herzberg, A. Hauptmann, and S. J. Hamilton. Domain independent post-processing with graph U-nets: applications to electrical impedance tomographic imaging. *Physiol. Meas.*, 44(12):125008, 2023. doi: 10.1088/1361-6579/ad0b3d. URL <https://dx.doi.org/10.1088/1361-6579/ad0b3d>.
- D. S. Holder, editor. *Electrical Impedance Tomography: Methods, History and Applications*. Institute of Physics Publishing, Bristol, 2004.
- S.-W. Huang, H.-M. Cheng, and S.-F. Lin. Improved imaging resolution of electrical impedance tomography using artificial neural networks for image reconstruction. In *2019 41st Annual International Conference of the IEEE Engineering in Medicine and Biology Society (EMBC)*, pages 1551–1554. IEEE, 2019.
- N. Hyvönen. Complete electrode model of electrical impedance tomography: approximation properties and characterization of inclusions. *SIAM J. Appl. Math.*, 64(3):902–931, 2004. ISSN 0036-1399,1095-712X. doi: 10.1137/S0036139903423303. URL <https://doi.org/10.1137/S0036139903423303>.
- N. Hyvönen. Approximating idealized boundary data of electric impedance tomography by electrode measurements. *Math. Models Methods Appl. Sci.*, 19(07):1185–1202, 2009.
- N. Hyvönen and L. Mustonen. Smoothened complete electrode model. *SIAM J. Appl. Math.*, 77(6):2250–2271, 2017.
- M. Ikehata. Reconstruction of the shape of the inclusion by boundary measurements. *Commun. Partial Diff. Equ.*, 23(7-8):1459–1474, 1998.
- V. Isakov. *Inverse Problems for Partial Differential Equations*. Springer, New York, 2nd edition, 2006. ISBN 978-0387-25364-0; 0-387-25364-5.
- K. Ito and B. Jin. *Inverse problems: Tikhonov theory and algorithms*. World Scientific Publishing Co. Pte. Ltd., Hackensack, NJ, 2015. ISBN 978-981-4596-19-0.
- K. Ito, B. Jin, and J. Zou. A direct sampling method to an inverse medium scattering problem. *Inverse Problems*, 28(2):025003, 11, 2012. ISSN 0266-5611,1361-6420. doi: 10.1088/0266-5611/28/2/025003. URL <https://doi.org/10.1088/0266-5611/28/2/025003>.
- K. Ito, B. Jin, F. Wang, and J. Zou. Iterative direct sampling method for elliptic inverse problems with limited Cauchy data. *SIAM J. Imaging Sci.*, 18(2):1284–1313, 2025. ISSN 1936-4954. doi: 10.1137/24M1716756. URL <https://doi.org/10.1137/24M1716756>.
- B. Jin and P. Maass. An analysis of electrical impedance tomography with applications to tikhonov regularization. *ESAIM: Control, Optim. Cal. Var.*, 18(4):1027–1048, 2012.
- B. Jin and Y. Xu. Adaptive reconstruction for electrical impedance tomography with a piecewise constant conductivity. *Inverse Problems*, 36(1):014003, 28, 2020. ISSN 0266-5611,1361-6420. doi: 10.1088/1361-6420/ab261e. URL <https://doi.org/10.1088/1361-6420/ab261e>.
- B. Jin, T. Khan, P. Maass, and M. Pidcock. Function spaces and optimal currents in impedance tomography. *J. Inverse Ill-Posed Probl.*, 19(1):25–48, 2011. ISSN 0928-0219,1569-3945. doi: 10.1515/JIIP.2011.022. URL <https://doi.org/10.1515/JIIP.2011.022>.

- B. Jin, T. Khan, and P. Maass. A reconstruction algorithm for electrical impedance tomography based on sparsity regularization. *Internat. J. Numer. Methods Engrg.*, 89(3):337–353, 2012. ISSN 0029-5981,1097-0207. doi: 10.1002/nme.3247. URL <https://doi.org/10.1002/nme.3247>.
- B. Jin, Y. Xu, and J. Zou. A convergent adaptive finite element method for electrical impedance tomography. *IMA J. Numer. Anal.*, 37(3):1520–1550, 2017. ISSN 0272-4979,1464-3642. doi: 10.1093/imanum/drw045. URL <https://doi.org/10.1093/imanum/drw045>.
- J. P. Kaipio, V. Kolehmainen, E. Somersalo, and M. Vauhkonen. Statistical inversion and Monte Carlo sampling methods in electrical impedance tomography. *Inverse Problems*, 16(5):1487–1522, 2000. ISSN 0266-5611,1361-6420. doi: 10.1088/0266-5611/16/5/321. URL <https://doi.org/10.1088/0266-5611/16/5/321>.
- B. Kaltenbacher, A. Neubauer, and O. Scherzer. *Iterative regularization methods for nonlinear ill-posed problems*. Walter de Gruyter GmbH & Co. KG, Berlin, 2008. ISBN 978-3-11-020420-9. doi: 10.1515/9783110208276. URL <https://doi.org/10.1515/9783110208276>.
- K. Karhunen, A. Seppänen, A. Lehikoinen, P. J. Monteiro, and J. P. Kaipio. Electrical resistance tomography imaging of concrete. *Cement Concr. Res.*, 40(1):137–145, 2010.
- T. A. Khan and S. H. Ling. Review on electrical impedance tomography: Artificial intelligence methods and its applications. *Algorithms*, 12(5):88, 2019.
- D. P. Kingma and J. Ba. Adam: A method for stochastic optimization. In *3rd International Conference for Learning Representations*, San Diego, 2015.
- D. P. Kingma and M. Welling. Auto-encoding variational bayes. In Y. Bengio and Y. LeCun, editors, *2nd International Conference on Learning Representations, ICLR 2014, Banff, AB, Canada, April 14–16, 2014, Conference Track Proceedings*, 2014.
- A. Kirsch. Characterization of the shape of a scattering obstacle using the spectral data of the far field operator. *Inverse Problems*, 14(6):1489–1512, 1998. ISSN 0266-5611,1361-6420. doi: 10.1088/0266-5611/14/6/009. URL <https://doi.org/10.1088/0266-5611/14/6/009>.
- M. B. Kiss, A. Biguri, Z. Shumaylov, F. Sherry, K. J. Batenburg, C.-B. Schönlieb, and F. Lucka. Benchmarking learned algorithms for computed tomography image reconstruction tasks. *Appl. Math. Mod. Chall.*, 3(0):1–43, 2025. doi: 10.3934/ammc.2025001. URL <https://www.aims sciences.org/article/id/67ab0b783942fc6603063e6e>.
- K. Knudsen and A. K. Rasmussen. Direct regularized reconstruction for the three-dimensional Calderón problem. *Inverse Probl. Imaging*, 16(4):871–894, 2022. ISSN 1930-8337,1930-8345. doi: 10.3934/ipi.2022002. URL <https://doi.org/10.3934/ipi.2022002>.
- K. Knudsen and A. Tamasan. Reconstruction of less regular conductivities in the plane. *Commun. Part. Diff. Equ.*, 29(3-4):361–381, 2005. ISSN 15324133, 03605302. doi: 10.1081/pde-120030401.
- K. Knudsen, M. Lassas, J. L. Mueller, and S. Siltanen. D-bar method for electrical impedance tomography with discontinuous conductivities. *SIAM J. Appl. Math.*, 67(3):893–913, 2007. ISSN 0036-1399,1095-712X. doi: 10.1137/060656930. URL <https://doi.org/10.1137/060656930>.
- K. Knudsen, M. Lassas, J. L. Mueller, and S. Siltanen. Regularized D-bar method for the inverse conductivity problem. *Inverse Probl. Imaging*, 3(4):599–624, 2009. ISSN 1930-8337,1930-8345. doi: 10.3934/ipi.2009.3.599. URL <https://doi.org/10.3934/ipi.2009.3.599>.
- J. Kourunen, T. Savolainen, A. Lehikoinen, M. Vauhkonen, and L. Heikkinen. Suitability of a pxi platform for an electrical impedance tomography system. *Meas. Sci. Technol.*, 20(1):015503, 2008.
- A. Lechleiter. The MUSIC algorithm for impedance tomography of small inclusions from discrete data. *Inverse Problems*, 31(9):095004, 19, 2015. ISSN 0266-5611,1361-6420. doi: 10.1088/0266-5611/31/9/095004. URL <https://doi.org/10.1088/0266-5611/31/9/095004>.
- A. Lechleiter and A. Rieder. Newton regularizations for impedance tomography: a numerical study. *Inverse Problems*, 22(6):1967–1987, 2006. ISSN 0266-5611,1361-6420. doi: 10.1088/0266-5611/22/6/004. URL <https://doi.org/10.1088/0266-5611/22/6/004>.
- A. Lechleiter and A. Rieder. Newton regularizations for impedance tomography: convergence by local injectivity. *Inverse Problems*, 24(6):065009, 18, 2008. ISSN 0266-5611,1361-6420. doi: 10.1088/0266-5611/24/6/065009. URL <https://doi.org/10.1088/0266-5611/24/6/065009>.
- A. Lechleiter and A. Rieder. Towards a general convergence theory for inexact Newton regularizations. *Numer. Math.*, 114(3):521–548, 2010. ISSN 0029-599X,0945-3245. doi: 10.1007/s00211-009-0256-0. URL <https://doi.org/10.1007/s00211-009-0256-0>.

- J. Leuschner, M. Schmidt, P. S. Ganguly, V. Andriiashen, S. B. Coban, A. Denker, D. Bauer, A. Hadjifaradji, K. J. Batenburg, P. Maass, et al. Quantitative comparison of deep learning-based image reconstruction methods for low-dose and sparse-angle ct applications. *J. Imag.*, 7(3):44, 2021.
- K. Levenberg. A method for the solution of certain non-linear problems in least squares. *Quart. Appl. Math.*, 2:164–168, 1944. ISSN 0033-569X,1552-4485. doi: 10.1090/qam/10666. URL <https://doi.org/10.1090/qam/10666>.
- K. Li, K. Shin, and Z. Zhou. Learning-enhanced variational regularization for electrical impedance tomography via Calderón’s method. Preprint, arXiv:2507.06114, 2025.
- X. Li, Y. Lu, J. Wang, X. Dang, Q. Wang, X. Duan, and Y. Sun. An image reconstruction framework based on deep neural network for electrical impedance tomography. In *2017 IEEE International Conference on Image Processing (ICIP)*, pages 3585–3589. IEEE, 2017.
- D. Liu, J. Wang, Q. Shan, D. Smyl, J. Deng, and J. Du. Deepeit: deep image prior enabled electrical impedance tomography. *IEEE Trans. Pattern Anal. Mach. Intell.*, 45(8):9627–9638, 2023. doi: 10.1109/TPAMI.2023.3240565.
- F. Margotti. Inexact Newton regularization combined with gradient methods in Banach spaces. *Inverse Problems*, 34(7):075007, 26, 2018. ISSN 0266-5611,1361-6420. doi: 10.1088/1361-6420/aac21f. URL <https://doi.org/10.1088/1361-6420/aac21f>.
- F. Margotti and E. Hafemann. Range-relaxed strategy applied to the Levenberg-Marquardt method with uniformly convex penalization term in Banach spaces. *Inverse Problems*, 38(9):095001, 35, 2022. ISSN 0266-5611,1361-6420. doi: 10.1088/1361-6420/ac7e68. URL <https://doi.org/10.1088/1361-6420/ac7e68>.
- F. J. Margotti. *On inexact Newton methods for inverse problems in Banach spaces*. PhD thesis, Karlsruhe, Karlsruher Institut für Technologie (KIT), Diss., 2015, 2015.
- D. W. Marquardt. An algorithm for least-squares estimation of nonlinear parameters. *J. Soc. Indust. Appl. Math.*, 11:431–441, 1963. ISSN 0368-4245.
- S. Martin and C. T. Choi. A post-processing method for three-dimensional electrical impedance tomography. *Sci. Rep.*, 7(1):7212, 2017.
- N. G. Meyers. An  $L^p$ e-estimate for the gradient of solutions of second order elliptic divergence equations. *Ann. Scuola Norm. Sup. Pisa Cl. Sci. (3)*, 17:189–206, 1963. ISSN 0391-173X.
- M. Mozumder, A. Hauptmann, I. Nissilä, S. R. Arridge, and T. Tarvainen. A model-based iterative learning approach for diffuse optical tomography. *IEEE Trans. Med. Imag.*, 41(5):1289–1299, 2021.
- J. L. Mueller and S. Siltanen. The D-bar method for electrical impedance tomography—demystified. *Inverse Problems*, 36(9):093001, 28, 2020. ISSN 0266-5611,1361-6420. doi: 10.1088/1361-6420/aba2f5. URL <https://doi.org/10.1088/1361-6420/aba2f5>.
- A. I. Nachman. Reconstructions from boundary measurements. *Ann. of Math.* (2), 128(3):531–576, 1988. ISSN 0003-486X,1939-8980. doi: 10.2307/1971435. URL <https://doi.org/10.2307/1971435>.
- A. I. Nachman. Global uniqueness for a two-dimensional inverse boundary value problem. *Ann. of Math.* (2), 143(1):71–96, 1996. ISSN 0003-486X,1939-8980. doi: 10.2307/2118653. URL <https://doi.org/10.2307/2118653>.
- J. W. Neuberger. *Sobolev Gradients and Differential Equations*. Springer-Verlag, Berlin, 1997. ISBN 3-540-63537-8. doi: 10.1007/BFb0092831. URL <https://doi.org/10.1007/BFb0092831>.
- R. G. Novikov. A multidimensional inverse spectral problem for the equation  $-\Delta\psi + (v(x) - Eu(x))\psi = 0$ . *Funktional. Anal. i Prilozhen.*, 22(4):11–22, 96, 1988. ISSN 0374-1990. doi: 10.1007/BF01077418. URL <https://doi.org/10.1007/BF01077418>.
- S. Osher and J. A. Sethian. Fronts propagating with curvature-dependent speed: Algorithms based on Hamilton-Jacobi formulations. *J. Comput. Phys.*, 79(1):12–49, 1988. ISSN 0021-9991. doi: [https://doi.org/10.1016/0021-9991\(88\)90002-2](https://doi.org/10.1016/0021-9991(88)90002-2). URL <https://www.sciencedirect.com/science/article/pii/0021999188900022>.
- N. Otsu. A threshold selection method from gray-level histograms. *Automatica*, 11(285-296):23–27, 1975.
- A. Pokkunuru, P. Rooshenas, T. Strauss, A. Abhishek, and T. Khan. Improved training of physics-informed neural networks using energy-based priors: a study on electrical impedance tomography. In *The Eleventh International Conference on Learning Representations*, 2022.
- N. Polydorides and W. R. B. Lionheart. A Matlab toolkit for three-dimensional electrical impedance tomography: a contribution to the electrical impedance and diffuse optical reconstruction software project. *Meas. Sci. Technol.*, 13(12):1871–1883, 2002. doi: 10.1088/0957-0233/13/12/310. URL <https://dx.doi.org/10.1088/0957-0233/13/12/310>.

- M. Raissi, P. Perdikaris, and G. E. Karniadakis. Physics-informed neural networks: A deep learning framework for solving forward and inverse problems involving nonlinear partial differential equations. *J. Comput. Phys.*, 378: 686–707, 2019.
- A. Rieder. On the regularization of nonlinear ill-posed problems via inexact Newton iterations. *Inverse Problems*, 15(1):309–327, 1999. ISSN 0266-5611,1361-6420. doi: 10.1088/0266-5611/15/1/028. URL <https://doi.org/10.1088/0266-5611/15/1/028>.
- O. Ronneberger, P. Fischer, and T. Brox. U-net: Convolutional networks for biomedical image segmentation. In *Medical Image Computing and Computer-Assisted Intervention—MICCAI 2015: 18th International Conference, Munich, Germany, October 5–9, 2015, Proceedings, Part III* 18, pages 234–241. Springer, 2015a.
- O. Ronneberger, P. Fischer, and T. Brox. U-net: Convolutional networks for biomedical image segmentation. In *International Conference on Medical Image Computing and Computer-Assisted Intervention*, pages 234–241. Springer, 2015b.
- L. I. Rudin, S. Osher, and E. Fatemi. Nonlinear total variation based noise removal algorithms. *Physica D: Nonlin. Phen.*, 60(1-4):259–268, 1992.
- M. Räsänen, P. Kuusela, J. Jauhainen, M. Arif, K. Scheel, T. Savolainen, and A. Seppänen. Kuopio tomography challenge 2023 – electrical impedance tomography competition and open dataset. *Appl. Math. Mod. Chall.*, 2(2):93–118, 2024. doi: 10.3934/ammc.2024009. URL <https://www.aims sciences.org/article/id/666ab5a65a42b314c5bf2ea5>.
- F. Santosa. A level-set approach for inverse problems involving obstacles. *ESAIM: Control, Optimisation and Calculus of Variations*, 1:17–33, 1995/96. ISSN 1292-8119,1262-3377. doi: 10.1051/cocv:1996101. URL <https://doi.org/10.1051/cocv:1996101>.
- J. Seo, K. Kim, A. Jargal, K. Lee, and B. Harrach. A learning-based method for solving ill-posed nonlinear inverse problems: A simulation study of lung eit. *SIAM J. Imaging Sci.*, 12(3):1275–1295, 2019. ISSN 1936-4954. doi: 10.1137/18M1222600.
- K. Shin and J. L. Mueller. A second order Calderón’s method with a correction term and *a priori* information. *Inverse Problems*, 36(12):124005, 22, 2020. ISSN 0266-5611,1361-6420. doi: 10.1088/1361-6420/abb014. URL <https://doi.org/10.1088/1361-6420/abb014>.
- S. Siltanen, J. Mueller, and D. Isaacson. An implementation of the reconstruction algorithm of A. Nachman for the 2D inverse conductivity problem. *Inverse Problems*, 16(3):681–699, 2000. ISSN 0266-5611,1361-6420. doi: 10.1088/0266-5611/16/3/310. URL <https://doi.org/10.1088/0266-5611/16/3/310>.
- S. Sippola, S. Rautio, A. Hauptmann, T. Ide, and S. Siltanen. Learned enclosure method for experimental eit data. *Appl. Math. Modern Chall.*, 4:47–65, 2025.
- D. Smyl, T. N. Tallman, D. Liu, and A. Hauptmann. An efficient quasi-newton method for nonlinear inverse problems via learned singular values. *IEEE Signal Proc. Lett.*, 28:748–752, 2021.
- E. Somersalo. Locating anisotropy in electrical impedance tomography. *arXiv preprint arXiv:math/0110299v1*, 2001.
- E. Somersalo, M. Cheney, and D. Isaacson. Existence and uniqueness for electrode models for electric current computed tomography. *SIAM J. Appl. Math.*, 52(4):1023–1040, 1992. ISSN 0036-1399. doi: 10.1137/0152060. URL <https://doi.org/10.1137/0152060>.
- Y. Song, J. Sohl-Dickstein, D. P. Kingma, A. Kumar, S. Ermon, and B. Poole. Score-based generative modeling through stochastic differential equations. In *9th International Conference on Learning Representations, ICLR 2021*. OpenReview.net, 2021.
- B. Sun, H. Zhong, Y. Zhao, L. Ma, and H. Wang. Calderón’s method-guided deep neural network for electrical impedance tomography. *IEEE Trans. Instrum. Meas.*, 72:4507911, 2023. doi: 10.1109/TIM.2023.3322501.
- C. Tan, S. Lv, F. Dong, and M. Takei. Image reconstruction based on convolutional neural network for electrical resistance tomography. *IEEE Sensors J.*, 19(1):196–204, 2018.
- D. N. Tanyu, J. Ning, A. Hauptmann, B. Jin, and P. Maass. Electrical impedance tomography: a fair comparative study on deep learning and analytic-based approaches. In T. Bubba, editor, *Data-driven Models in Inverse Problems*, pages 437–470. De Gruyter, Berlin, Boston, 2025. ISBN 9783111251233. doi: doi:10.1515/9783111251233-013. URL <https://doi.org/10.1515/9783111251233-013>.
- J. Toivanen, V. Kolehmainen, A. Paldanius, A. Hänninen, A. Hauptmann, and S. Hamilton. Graph convolutional networks enable fast hemorrhagic stroke monitoring with electrical impedance tomography. *IEEE Trans. Biomed. Eng.*, page in press, 2025.

- G. Uhlmann. Electrical impedance tomography and Calderón's problem. *Inverse Problems*, 25(12):123011, 39, 2009. ISSN 0266-5611,1361-6420. doi: 10.1088/0266-5611/25/12/123011. URL <https://doi.org/10.1088/0266-5611/25/12/123011>.
- D. Ulyanov, A. Vedaldi, and V. Lempitsky. Deep image prior. In *Proceedings of the IEEE Conference on Computer Vision and Pattern Recognition*, pages 9446–9454, 2018.
- C. R. Vogel and M. E. Oman. Iterative methods for total variation denoising. *SIAM J. Sci. Comput.*, 17(1):227–238, 1996.
- H. Wang, G. Xu, and Q. Zhou. A comparative study of variational autoencoders, normalizing flows, and score-based diffusion models for electrical impedance tomography. *J. Inverse Ill-posed Probl.*, 32(4):795–813, 2024. doi: doi:10.1515/jiip-2023-0037. URL <https://doi.org/10.1515/jiip-2023-0037>.
- Z. Wei, D. Liu, and X. Chen. Dominant-current deep learning scheme for electrical impedance tomography. *IEEE Trans. Biomed. Eng.*, 66(9):2546–2555, 2019.
- R. Williams and M. Beck, editors. *Process Tomography: Principles, Techniques and Applications*. Butterworth-Heinemann, Oxford, 1995.
- S. J. Wright, R. D. Nowak, and M. A. T. Figueiredo. Sparse reconstruction by separable approximation. *IEEE Trans. Signal Process.*, 57(7):2479–2493, 2009. ISSN 1053-587X,1941-0476. doi: 10.1109/TSP.2009.2016892. URL <https://doi.org/10.1109/TSP.2009.2016892>.
- D. Yang, S. Li, Y. Zhao, B. Xu, and W. Tian. An eit image reconstruction method based on densenet with multi-scale convolution. *Math. Biosci. Eng.*, 20(4):7633–7660, 2023.
- X. Zhang, Z. Wang, R. Fu, D. Wang, X. Chen, X. Guo, and H. Wang. V-shaped dense denoising convolutional neural network for electrical impedance tomography. *IEEE Trans. Instrum. Meas.*, 71:1–14, 2022.